Copy 710

[redacted] NASA TM X-77

NASA TM X-77

FACILITY FORM 602

N65-28448	
(ACCESSION NUMBER)	(THRU)
48	1
(PAGES)	(CODE)
	33
(NASA CR OR TMX OR AD NUMBER)	(CATEGORY)

TECHNICAL MEMORANDUM

X-77

DECLASSIFIED BY AUTHORITY OF NASA
CLASSFICATION CHANGE NOTICES NO. 12
DATED 5-26-65 ITEM NO. 26

HEAT-TRANSFER MEASUREMENTS ON A BLUNT SPHERICAL-SEGMENT NOSE TO A MACH NUMBER OF 15.1 AND FLIGHT PERFORMANCE OF THE ROCKET-PROPELLED MODEL TO A MACH NUMBER OF 17.8

By Charles B. Rumsey and Dorothy B. Lee

Langley Research Center
Langley Field, Va.

GPO PRICE $ ________

OTS PRICE(S) $ ________

Hard copy (HC) 2.00

Microfiche (MF) .50

DECLASSIFIED: EFFECTIVE 4-29-65
AUTHORITY F.G. DROBKA (ATSS-A)
TO dated 5-13-65: AFSDO 5439

[redacted]

NATIONAL AERONAUTICS AND SPACE ADMINISTRATION
WASHINGTON November 1959

[redacted]

1D

DECLASSIFIED

CONFIDENTIAL

NATIONAL AERONAUTICS AND SPACE ADMINISTRATION

TECHNICAL MEMORANDUM X-77

HEAT-TRANSFER MEASUREMENTS ON A BLUNT SPHERICAL-SEGMENT NOSE TO A MACH NUMBER OF 15.1 AND FLIGHT PERFORMANCE OF THE ROCKET-PROPELLED MODEL TO A MACH NUMBER OF 17.8*

By Charles B. Rumsey and Dorothy B. Lee

DECLASSIFIED BY AUTHORITY OF NASA
CLASSIFICATION CHANGE NOTICES NO. 2
DATED 5-26-65 ITEM NO. 26

28448

SUMMARY

A five-stage rocket-propelled model was flight tested to a Mach number of 17.8 and heat-transfer measurements were obtained on the blunt spherical-segment nose and cylindrical body to a Mach number of 15.1 at a Reynolds number of 0.77×10^6 based on nose diameter. The ratio of nose radius to radius of curvature was 0.444.

At and near the stagnation point, the experimental heating rates agreed within 20 percent with theoretical laminar rates for equilibrium dissociated air. At other locations on the spherical-segment face the experimental values differed by as much as 50 percent from the distribution predicted by a simplified theory for laminar flow. On the cylindrical body, within 0.29 diameter of the corner, the experimental heating rates were roughly 10 percent of the stagnation-point rates.

INTRODUCTION

Aerodynamic heat transfer to bodies and nose shapes in free flight at supersonic speeds has been the subject of a series of investigations carried on by the Langley Pilotless Aircraft Research Division using multistage solid-fuel rocket-propelled models. The investigations have been made at progressively higher speeds through the use of additional stages and larger rocket motors. Investigations of heat transfer to several nose shapes at Mach numbers up to 14 which utilized a five-stage rocket-motor system consisting of Honest John, Nike, Nike, Recruit, and T55 motors have been previously reported (refs. 1 to 4). In order to

---

*Title, Unclassified.

[redacted]

provide a means for obtaining heat transfer and other aerodynamic information in free flight at higher supersonic speeds, a five-stage vehicle was devised utilizing the Sergeant motor as the first stage. With this vehicle, Mach numbers of about 18 are obtainable on trajectories suitable for heat-transfer studies.

The first use of this vehicle was for the investigation of heat transfer to a blunt spherical-segment nose shape for which the theoretical distribution of heat transfer is essentially constant over the spherical portion. Heat-transfer data were obtained to Mach number 15.1 and are presented herein. Because of the telemeter-signal failure, data were not obtained to maximum Mach number, but the results indicate that the model reached a Mach number of 17.8 at an altitude of 94,000 feet.

L
6
1
7

Also presented herein are some pertinent mechanical details of the configuration and techniques of the flight test which was conducted at the NASA Wallops Station.

SYMBOLS

A_{n+1}	contact area between elements n and n + 1, sq ft
A_{n-1}	contact area between elements n and n - 1, sq ft
a	speed of sound, ft/sec
c_p	specific heat of air, Btu/(lb)(°F)
D	nose diameter, ft
g	gravitational constant, 32.2 ft/sec^2
h	aerodynamic heat-transfer coefficient, Btu/(sq ft)(sec)(°F)
h_w	enthalpy at wall temperature, Btu/lb
h_{total}	total enthalpy, Btu/lb
k	conductivity, (Btu)(ft)/(sec)(°F)(sq ft)
M	Mach number
N_{Nu}	Nusselt number

[redacted]

N_{St}	Stanton number
N_{Pr}	Prandtl number
p	pressure, lb/sq ft
q	heating rate, Btu/(sec)(sq ft)
R_D	free-stream Reynolds number based on nose diameter
R	Reynolds number
r	radius of nose, 2.6 in.
r'	radius of curvature, 5.85 in.
S	length of arc along spherical-segment nose, ft
ΔS_{n+1}	distance between thermocouple locations in elements n and $n+1$, ft
ΔS_{n-1}	distance between thermocouple locations in elements n and $n-1$, ft
T	temperature, °R unless otherwise noted
t	time, sec
V	velocity, ft/sec
x	length from corner along cylinder to measurement point, ft
Z_n	area of element n exposed to airflow, sq ft
γ	ratio of specific heats of air
μ	viscosity of air, slugs/ft-sec
ρ	density of air, slugs/cu ft

Subscripts:

aw	adiabatic wall
exp	experimental
l	local

[redacted]

lat	lateral
max	maximum
t	stagnation
w	wall
∞	free stream

MODEL AND TESTS

Model

The model, or fifth stage, was a body of revolution, 66.4 inches long, with a blunt spherical-segment nose, a stepped cylindrical midsection, and a 10° half-angle flare section at the rear. Figure 1 shows dimensions of the model and pertinent details of the nose on which the skin-temperature measurements were made. A photograph of the model is shown in figure 2.

The test nose consisted of a spherical-segment face followed by a short cylindrical section. The spherical segment was machined 1/2 inch thick from high-conductivity, oxygen-free copper and was welded to the cylinder which was spun from 0.05-inch-thick Inconel. The copper surface was finished with fine-grit sandpaper and buffed with jeweler's rouge with no particular effort made to attain a high-quality finish. The surface roughness was estimated, using an interference microscope, to be 15 to 20 microinches with several fine scratches which were very likely much deeper than 20 microinches.

The stepped cylindrical midsection of the model was spun from 0.031-inch-thick Inconel and chemically milled back of the step to a thickness of 0.02 inch. The midsection skin was free to expand rearward and the back end of the skin slipped over a short cylindrical section in front of the flare.

The flare, which provided aerodynamic stability for the model, was constructed of 0.091-inch-thick Inconel. It was attached at its front end to the throat section of the rocket motor nozzle. The nozzle extended to the base of the flare where its diameter was approximately 2 inches less than the flare diameter.

The telemeter equipment was carried inside the cylindrical part of the model ahead of the step and was protected from the high skin temperatures by a radiation shield. The fifth-stage rocket motor was located in the cylindrical part of the body behind the step.

[redacted]

Instrumentation

The telemeter, which was carried in the forward part of the model and protected from the skin temperature by a heat shield, transmitted six channels of information. These were normal and transverse accelerations, thrust and drag accelerations, and two channels of skin-temperature information. Readings from 13 skin-temperature thermocouples were commutated on the two temperature channels. The locations of the 13 thermocouple stations are shown in figure 1(a). Eight of the thermocouples were located in a line along one element of the nose (six were located on the spherical portion and two were located on the cylinder). The other five (three were located on the spherical portion and two were located on the cylinder) were located along other elements to determine the symmetry of the heating.

The commutation arrangement was such that the thermocouples on the copper face were sampled approximately 10 times a second and those on the cylindrical section were sampled half as often. Three constant voltages were also commutated at the slower rate on each of the thermocouple channels. The constant voltages were chosen to be equivalent to the lowest, middle, and highest temperatures anticipated (80° to $1,900^{\circ}$ F) and provided an inflight calibration of the thermocouple telemetering system.

Installation of the thermocouples, which were made of No. 30 chromel-alumel wire, was by three different methods. Those installed on the Inconel cylindrical section were spot welded to the inner surface of the skin. Both peened and plug type of installations were used on the 1/2-inch-thick copper spherical-segment nose. For the three peened installations, a hole, just sufficiently deep to accept the thermocouple bead, was drilled into the inner surface and the surface was then peened around the bead. The six plug type of thermocouples were made by installing copper-sheathed, ceramic-insulated thermocouple wire in copper plugs accurately machined from the same material as the nose; the plugs were then pressed into holes bored in the spherical-segment nose. (See fig. 1(b).) In order to install the thermocouple in the plug, the copper sheathing and ceramic insulation were trimmed back 0.01 inch from the end of the thermocouple wires. The plug was then heated with a small amount of high-temperature silver solder in the bottom of the hole and the sheath was carefully inserted until the thermocouple wires bottomed. Each plug was X-rayed after installation of the thermocouple and was used only if no gas pocket or other flow was discernible. Construction and installation of the plugs were such that the bottom of the hole was 0.05 (+0, -0.002) inch from the finished outside surface. The thermocouple readings were assumed to be the temperatures at 0.05 inch (or 10 percent of the skin thickness) from the heated face.

Thrust and drag accelerations were measured continuously by accelerometers calibrated in gravitational units from -1 g to 140g units of thrust and from 1 g to -35g units of drag. Normal and transverse accelerations were measured continuously by accelerometers calibrated to ±20g.

[redacted]

Telemetering receiving stations were located at the launching site (NASA Wallops Station) and on a ship 35 miles down range from the launching site.

A modified AN/DPN-19 radar beacon was carried in the adapter between the third and fourth stages. It extended the range of the NACA modified SCR-584 tracking radar data and provided a means of firing the second-stage motor, as will be discussed subsequently. The tracking radar provided the time history of the model in space up to the fourth-stage firing. When the fourth stage ignited, the beacon was, of course, destroyed; since the range was then too great for skin tracking by the NACA modified SCR-584 radar set, no radar data were obtained beyond this point.

Atmospheric conditions were obtained from Rawinsonde measurements to an altitude of 93,000 feet where the measured data were in close agreement with standard altitude conditions. Standard atmospheric tables (ref. 5) were used for altitudes from 93,000 feet to the peak altitude of 111,600 feet.

Booster Stages and Test Techniques

The five-stage propulsion system consisted of seven solid-fuel rocket motors. The first stage was a Sergeant XM20 motor with two Recruit XM19 motors fastened on opposite sides between the Sergeant fins. The second and third stages were Lance XM25 motors, the fourth stage was a Recruit XM19, and the fifth-stage motor, which was carried inside the model, was a T55. The stages were locked together, except for the first and second stages, by blowout diaphragms designed to allow each stage to blast off the expended preceding stage. The first stage was locked to the second by a locking-band and explosive-bolt arrangement. Figure 3 is a photograph of the complete configuration on the launcher, and figure 4 gives dimensions and details of the model-booster assembly and a table of pertinent characteristics of the motors.

The test technique was to launch the combination at 70° elevation and boost it to a Mach number of 3.1 with the long-burning Sergeant motor, allow the last four stages to coast to the peak altitude of 111,600 feet, and then fire these stages in rapid succession on a shallow reentry trajectory. Burnout Mach number was 17.8 at 93,700 feet altitude. Figure 5 shows altitude plotted against horizontal range of the flight.

The two Recruit motors, which burned only 1.9 seconds, were added to the first stage to increase the take-off acceleration of the 13,727-pound combination from 2.5g units (without Recruits) to 7.4g units. Dynamic trajectory computations showed that this increase in take-off g units would reduce appreciably the tip over during the low-speed period following take-off and thereby increase the peak altitude for the coasting stages from 75,000 feet (without Recruits) to 117,000 feet. (Peak

[redacted]

altitude attained was 5,400 feet less than this primarily because of the influence of atmospheric winds.)

The two Recruit Motors were fired by means of pull-away clips when the model began to move so that they would not ignite prior to the Sergeant ignition. Also, with this firing sequence the Sergeant motor was pressurized and therefore strengthened when the thrust of the Recruits was applied to the structure.

The Sergeant motor burned for 32 seconds. At 38 seconds it drag separated when delay squibs fired two explosive bolts releasing the locking-band arrangement. The remaining stages then coasted through peak altitude.

After ignition of the second stage just past peak altitude (as discussed subsequently), the third, fourth, and fifth stages were fired automatically at burnout of the previous stage by means of pressure switches cocked and tripped by the rise and fall, respectively, of the chamber pressure of the motor of the previous stage.

The critical ignition was that of the second stage. In order to obtain maximum Mach number without overheating the structure of the model, a reentry trajectory with fifth-stage burnout at about 95,000 feet was desired. Preflight computations showed that atmospheric winds and relatively small variations in Sergeant motor performance could vary the trajectory to such an extent that a mechanical timer for second-stage ignition could not be relied on to give the desired trajectory. Therefore, a ground command system was used to fire the second stage when the combination was at the altitude and reentry angle to give the desired burnout altitude. This point in the trajectory was determined by comparing the flight trajectory as it progressed on the radar plot board with previously computed trajectories.

The command system operated through the radar beacon (carried in the third stage) by coding the radar signal and thereby causing the beacon to activate a switch which fired the second stage. A mechanical timer kept the switch unarmed until a time approaching peak altitude because the severe vibrations during Sergeant burning were capable of prematurely activating the switch. The mechanical timer also included a "backup" firing system so that in the event of a beacon or radar signal failure the last four stages would not go unfired. This part of the timer was set to fire the second stage at the latest time that could reasonably be expected for command system use. The timer was set at 76 seconds for aiming and 120 seconds for backup firing. The command system was actuated at 97.5 seconds and the resulting trajectory had a burnout altitude of 94,000 feet which was close to the desired burnout altitude of 95,000 feet.

[redacted]

RESULTS AND DISCUSSION

Performance

The velocity-time history of the test is shown in figures 6(a) and 6(b). Mach number and Reynolds number per foot are shown in figure 6(c). Peak Mach number was 17.8 at a Reynolds number per foot of 2.6×10^6. The curves are dashed after fifth-stage ignition to indicate that performance during this stage was not measured but is inferred as discussed below.

Velocity was obtained from differentiation of the radar tracking data until separation of the third stage in which the radar beacon was located. After ignition of the second stage, velocity was also determined from integration of the telemetered accelerations which was the most sensitive method for the thrusting period. However, the velocities from the two sources are in good agreement as shown in figure 6(b).

Although the telemeter signal failed at fifth-stage ignition, a short burst of signal (0.1 sec) was received approximately one-fourth of the way through burning of the stage. Normal, transverse, and thrust accelerations were recorded during this short period as well as one sampling of most of the commutated temperatures. Since normal and transverse accelerations indicated less than 1° angle of attack and the thrust value was close to that anticipated, it is believed the model performed satisfactorily. Velocity was therefore computed for the fifth stage by using previously measured flight performance of a T55 motor as described below.

Figure 7 shows the short burst of telemetered accelerometer data on a time scale plotted from the start of fifth-stage firing. Also shown are the accelerations recorded during burning of a similar fifth stage of a five-stage combination consisting of an Honest John, Nike, Nike, Recruit, and T55 (ref. 4). Accelerations of the present model are lower, as expected, because of differences in model drag coefficients, dynamic pressures, and model weights. The actual difference of 11g units was close to that anticipated (about 14g units). The dashed curve shows the presumed time history of acceleration which was integrated to obtain the fifth-stage performance.

Aerodynamic Heating

Since very low aerodynamic heating occurred during the earlier portions of the test, the heat-transfer data are considered only during the high-speed reentry portion of the trajectory after 104 seconds. The

[redacted]

test conditions for this part of the flight are given in figures 8 and 9 which show time histories of velocity, altitude, Mach number, free-stream Reynolds number based on the nose diameter of 5.2 inches, and the ambient values of velocity of sound, density, temperature, and pressure.

Skin temperatures.- The skin temperatures measured on the nose and cylinder along the primary ray of thermocouples are shown in figure 10. The temperatures measured within the skin 0.05 inch from the outside (heated) surface by the plug thermocouple installations are shown in figure 10(a). These temperatures are hotter by as much as 200° F than those measured by thermocouples peened to the inside surface of the copper, which are shown in figure 10(b). Temperatures measured at the two cylinder stations along the primary ray are also shown in figure 10(b).

Figures 11(a) and 11(b) show typical temperature-time histories for the inside and outside skin on the copper nose and Inconel cylinder. The solid curve in each case is the faired measurement taken from figure 10.

For plug-type installations outside and inside surface temperatures were computed from the measurements using Hill's method (ref. 6). Since the method shows a tendency towards instability when time intervals which are too small are used, two sets of computations were made at interspaced time intervals in order to obtain close time spacing. Similar computations were made for outside surface temperatures on the Inconel cylinder.

For the peened type of installation on the 1/2-inch-thick copper nose, an indirect method was necessary to determine the outside surface temperature since Hill's method tended toward gross instability when used with reasonably small time intervals because of the high heating rates and the large thermal thickness. An estimate of the outside-surface-temperature—time history was made from which inside surface temperatures were computed using Hill's method. (Computations of inner surface temperatures from temperatures of the heated surface have no tendency towards instability.) Repeated estimates and many refairings were made until the outside-surface-temperature—time history was found which produced an inside-surface temperature within 1° of the measured temperature. Duplicate computations made at interspaced time intervals also produced the inside surface temperature within 1° of the measured temperature. The outside surface temperatures for all thermocouple locations are presented in table I.

Distributions of inside and outside surface temperatures along the nose are shown in figure 12(a) for three typical times during the test. Straight lines are used to connect the data points only to aid in distinguishing the different sets of data. Figure 12(b) shows distributions along the nose of the average wall temperature at each station, where the average temperature is assumed to be the inside surface temperature plus one-third the temperature increase from inside to outside surface. This assumption is correct for a condition of linear increase in heating rate with time (ref. 7). Figures 12(a) and 12(b) show relatively low temperatures at stations 4 and 5_a ($S/S_{max} = 0.57$ and 0.76). The thermocouple installations were of different types at these two adjacent stations (station 4 and 5_a are peen and plug installations, respectively) and the measured temperatures were different by as much as 130° F. (See fig. 12(a).) It is noteworthy that the surface temperatures at the two stations, although unexpectedly low, are in close agreement.

Heating rates.- One-dimensional heating rates were computed from the time histories of outside wall temperatures by means of the computational procedure of reference 6 in which only heat flow normal to the skin is considered. At stations on the spherical-segment face, these one-dimensional heating rates were modified by a first-order correction to account for the lateral conduction in the thick copper face caused by the temperature gradients across the face which are apparent in figure 12(b). No corrections were made to the one-dimensional results for stations on the cylindrical part of the nose since lateral conduction along the thin Inconel skin was negligible.

L
6
1
7

The method used to compute the corrections for lateral heat flow was similar to that used in reference 1. The nose was divided into annular rings, one for each thermocouple location, with the ring boundaries midway between thermocouples. The temperature of each ring was assumed to be the average temperature at the thermocouple location. The lateral heat-flow rates were then computed for the annular ring n by the equation

$$q_{n,lat} = \frac{k_s A_{n-1}(T_n - T_{n-1})}{Z_n \Delta S_{n-1}} + \frac{k_s A_{n+1}(T_n - T_{n+1})}{Z_n \Delta S_{n+1}} \qquad (1)$$

where $q_{n,lat}$ is given in Btu/(sec)(sq ft). The contact areas A_{n-1} and A_{n+1}, the lengths ΔS_{n-1} and ΔS_{n+1} to the adjacent thermocouples, and the area of the ring exposed to the airflow Z_n were determined from the dimensions of the nose and annular rings. Aerodynamic heating to the exposed cylindrical edge of the outermost annular ring and conduction between that ring and the Inconel cylindrical section of the nose were both neglected since estimates showed that results at the outermost-ring measurement station (station 6) were modified less than 6 percent by aerodynamic heating and less than 1 percent by the conduction.

The experimental aerodynamic heat-transfer rates were determined by adding, algebraically, the lateral heat-flow corrections for each station

[redacted]

to the corresponding one-dimensional heat-flow rates. Time histories of one-dimensional and aerodynamic heating rates measured on the spherical segment are presented in figures 13(a) to 13(c). The data points are given for both one-dimensional and aerodynamic rates to show the amount of scatter in the results and to show the magnitudes of the computed lateral heat flow.

The maximum aerodynamic heating rate, 867 Btu/(sec)(sq ft), occurred at station 3 which is 10° from the stagnation point, whereas the maximum one-dimensional heating rate of 731 Btu/(sec)(sq ft) occurred at the stagnation point (station 1). It may be noted that the one-dimensional rates are quite similar for four stations, 1 (stagnation point), 2_a, 3, and 6. The large lateral heat-flow corrections to stations 3 and 6 are due to the heat losses from these stations to stations 4 and 5_a where the heating rates were lower.

The heating rates on the cylindrical section of the nose, shown in figure 14, are roughly one-tenth of those on the spherical segment. Their comparison with theoretical estimates will be discussed later.

<u>Comparisons with theory</u>.- The experimental aerodynamic heating measured at the stagnation point (station 1) is compared in figure 15 with the theory of reference 8 for laminar stagnation-point heat transfer with equilibrium dissociation. This theory is expressed as

$$q_t = \frac{N_{Nu}}{\sqrt{R_w}} \frac{\sqrt{\rho_w \mu_w \left(\frac{dV}{dS}\right)_t}}{N_{Pr}} (h_{total} - h_w) \tag{2}$$

where

$$\frac{N_{Nu}}{\sqrt{R_w}} = 0.67\left(\frac{\rho_t \mu_t}{\rho_w \mu_w}\right)^{0.4} \tag{3}$$

for a Lewis number of 1 and a Prandtl number of 0.71.

The evaluations of density and temperature were made for the test conditions by assuming perfect-gas (constant value of c_p) relations behind a normal shock (ref. 9). As noted in reference 1, $\rho\mu$ values calculated using perfect-gas relations result in heating rates that are only 2 to 3 percent lower than those obtained using equilibrium-dissociation conditions. Sutherland's viscosity formula was used which is accurate within 10 percent for equilibrium air below 16,200° R

[redacted]

(ref. 8). For the present spherical-segment nose shapes, the term $\sqrt{(dV/dS)_t}$ was evaluated as 0.7 of $\sqrt{(dV/dS)_t}$ for a hemispherical nose of equal body diameter. The factor 0.7 was determined from the correlation of stagnation-point heat-transfer rates on spherical-segment nose shapes presented in reference 10. Values of $\sqrt{(dV/dS)_t}$ for a hemisphere as a function of Mach number were obtained from reference 1.

Figure 15 shows that after 108 seconds the theoretical laminar stagnation-point heating rates were in fair agreement (within 20 percent) with the experimental rates. Before 108 seconds (at Mach numbers less than 6.0), the heating rates were too low to have a reasonable percentage of accuracy.

L617

Distributions of experimental local heating rates on the spherical segment divided by the heating rates at the stagnation point are shown in figure 16 for Mach numbers 8.4 to 15.1. Also shown is the distribution given by the following relation for the ratio of local to stagnation-point heat-transfer coefficient:

$$\frac{h}{h_t} = \sqrt{\frac{\frac{V_l}{a_t}\left(\frac{p_l}{p_t}\right)^{1/2}\left(\frac{k_l}{k_t}\right)^2}{\frac{S}{r}\,\frac{r}{a_t}\left(\frac{dV}{dS}\right)_t}} \tag{4}$$

As shown in appendix C of reference 11, this expression, which neglects the effects of local pressure gradient, can be arrived at from the laminar heat-transfer relation

$$N_{St}\sqrt{R}(N_{Pr})^{2/3} = \text{Constant}$$

with the assumption that the ratio of local to stagnation-point Prandtl number is unity along the nose.

In evaluating equation (4), the pressure ratios (fig. 17) were obtained from reference 12 where the pressure distribution for this nose shape, obtained from shock-tube measurements, is presented. Values of k_l/k_t were assumed equal to the corresponding values of T_l/T_t, obtained directly from the pressure distribution, since T_l/T_t is within a few percent of unity except near the edge of the face. The pressure distribution was also used with the compressible Bernoulli equation

[redacted]

$$\frac{V_l}{a_t} = \sqrt{\frac{2}{\gamma - 1}\left[1 - \left(\frac{p_l}{p_t}\right)^{\frac{\gamma-1}{\gamma}}\right]}$$

to obtain the distribution of V_l/a_t along the nose. The slope of this distribution at the stagnation point provided a value for $\frac{r}{a_t}\left(\frac{dV}{dS}\right)_t$ of 0.58.

Reference 11 discusses the similarities between the simplified expression (eq. (4)) and the more refined expressions for laminar heating distributions of Lees (ref. 13) and Stine and Wanlass (ref. 14) and notes close agreement between equation (4) and Lees theory for the flat-faced-cylinder measurements of reference 11. Also, unpublished results from preflight jet measurements at NASA Wallops Station of pressure distributions and heat transfer at a Mach number of 2.0 on spherical-segment noses of various ratios of r/r' show that distributions from equation (4) fall between the distributions predicted for these tests by the equations of Lees and of Stine and Wanlass.

As shown in figure 16(a), equation (4) (ref. 11) gives a heating-rate distribution for the present nose shape which is almost constant and decreases only a few percent with distance from the stagnation point. The experimental rates show much more variation. At station 3 the rates are consistently above those at the stagnation point (station 1), being greater by as much as 33 percent, and at stations 4 and 5_a they are 25 to 50 percent less than the stagnation-point rates. The higher level of heating near the corner of the nose (station 6) does not appear to be the result of boundary-layer transition (note the higher level for turbulent flow at station 6 in fig. 16(a) computed by the theory of ref. 15 for $M = 15.1$) but may be due to the large pressure gradients near the corner and, in part, to the heating on the cylindrical edge of the copper nose.

The previously discussed corrections made to the one-dimensional heating rates to account for the conduction along the surface tend to magnify differences between the one-dimensional rates at adjacent stations. Thus, the high level of experimental heating rates at stations 3 and 6 and the low rates at their adjacent stations 4 and 5_a, could be taken as an indication that the conduction corrections computed by the finite-difference method used herein are too large. However, the uncorrected one-dimensional heating rates, which are plotted in figure 16(b), show that the heating at stations 4 and 5_a was quite low relative to the stagnation-point heating even if conduction is completely disregarded.

Figure 16(c) shows the experimental rates divided by q_t (the theoretical stagnation-point rates given in fig. 15). Since the theoretical

[redacted]

rates were generally somewhat less than the experimental rates at the stagnation point, the general level of the distribution is higher in figure 16(c) than in figure 16(a). However, the patterns shown in the two figures are similar, with the predominant characteristics being the relatively high level of heating 10° from the stagnation point (station 3) and the very much lower levels of heating 15° and 20° from the stagnation point (stations 4 and 5_a).

The heating rates measured on the cylinder are compared in figure 14 with Van Driest's flat-plate theory (ref. 16). Local conditions were determined using the assumptions of total pressure behind a normal shock, free-stream static pressure along the cylinder, and perfect-gas relations. The local Reynolds number was based on the distance from the corner of the nose to the cylindrical measurement station.

Because the local Reynolds numbers were very low ($0.004 \times 10^6 < R_2 < 0.011 \times 10^6$), the turbulent and laminar theoretical heating rates are similar. However, the theoretical values are fair approximations of the experimental measurements except at station 8_a where the measurements are higher by as much as 40 percent.

Symmetry of heating.- Five thermocouples were located to provide indications of the symmetry of the heating on the nose and cylinder. Three stations, 2_b, 5_b, and 8_b, were located diametrically opposite corresponding stations in the primary row of measurement stations. Two stations 5_c and 8_c were on a line 90° circumferentially from the primary and secondary rows. (See fig. 1.) Axisymmetric stations had the same type of thermocouple installations.

Figure 18 presents the heating rates at the axisymmetric stations. The rates are those obtained from the one-dimensional analysis. As previously noted, the influence of conduction is negligible for stations on the Inconel cylinder (stations 8_a, 8_b, and 8_c in fig. 18). Since conduction could not be computed for the isolated stations 2_b, 5_b, and 5_c on the copper nose, heating rates for these stations are compared with the one-dimensional rates for stations 2_a and 5_a.

No clear pattern is apparent in the asymmetries in heating rates shown in figure 18. Rates at station 2_b are lower than at station 2_a by as much as 31 percent, but at station 5_b they are higher than they are at station 5_a by as much as 23 percent. Rates at station 5_c are in good agreement with those at station 5_b. The telemetered normal and transverse accelerations, combined with estimated values of the lift-curve slope for the configuration, indicated angles of attack of up to 3° during the

[redacted]

first part of fourth-stage burning (110.52 to 111.5 seconds) and of about 1° or less thereafter. The orientation of the angle of attack remained consistently within about ±20° circumferentially and shifted the stagnation point toward station 2_b. Small effect would be expected on nose heating rates from angles of attack of those magnitudes. On the cylinder, the rates at stations 8_a and 8_c which agree well, are higher than those at station 8_b, diametrically opposite station 8_a. Since the angle of attack places station 8_a on the downwind side of the model, it would be expected to have the lower rate.

It may be noted here that if the previously discussed temperature and heat-transfer data for stations 4 and 5_a were disregarded and if the data from stations 5_b or 5_c were assumed to apply at the axisymmetric station 5_a, then the temperature distribution across the nose would be essentially flat. This in turn would greatly reduce the conduction corrections at stations 3 and 6, and result in a distribution of q across the nose (with no data at station 4) very similar to the theoretical distribution. No valid reason for disregarding the measurements at stations 4 and 5_a can be found however.

CONCLUDING REMARKS

A five-stage rocket-propelled model was flight tested to a Mach number of 17.8 at an altitude of 93,700 feet. Temperature measurements were made to a Mach number of 15.1 and a free-stream Reynolds number of 0.77×10^6 based on nose diameter at several locations on the blunt spherical-segment nose and immediately behind the nose on the cylindrical body.

At the stagnation point and at locations near the stagnation point, the experimental heating rates and theoretical values for laminar heating in equilibrium-dissociated air agreed within 20 percent. At other locations on the spherical-segment face the experimental values differed by as much as 50 percent from the essentially constant distribution of the ratio of local heating to stagnation-point heating predicted by a simplified theory for laminar flow. The data did not appear to indicate transitional or turbulent flow on the face.

On the cylinder immediately behind the nose the experimental heating rates were roughly one-tenth of the stagnation-point rates and were predicted within about 30 percent by laminar and turbulent flat-plate theories with Reynolds numbers based on length from the corner of the nose. Because these Reynolds numbers were very low the laminar and turbulent theoretical values were essentially the same.

Axisymmetric measurements made on the face at two distances from the stagnation point and on the cylindrical body at one axial location indicated that the heating was symmetrical around the nose within about 30 percent.

Langley Research Center,
National Aeronautics and Space Administration,
Langley Field, Va., July 8, 1959.

L
6
1
7

[redacted]

[redacted]

REFERENCES

1. Stoney, William E., Jr., and Swanson, Andrew G.: Heat Transfer Measured on a Flat-Face Cylinder in Free Flight at Mach Numbers up to 13.9. NACA RM L57E13, 1957.

2. Bland, William M., Jr., Rumsey, Charles B., Lee, Dorothy B., and Kolenkiewicz, Ronald: Free-Flight Aerodynamic-Heating Data to a Mach Number of 15.5 on a Blunted Conical Nose With a Total Angle of 29°. NACA RM L57F28, 1957.

3. Bland, William M., Jr., Swanson, Andrew G., and Kolenkiewicz, Ronald: Free-Flight Aerodynamic-Heating Data at Mach Numbers up to 10.9 on a Flat-Faced Cylinder. NACA RM L57K29, 1957.

4. Rumsey, Charles B., and Lee, Dorothy B.: Heat-Transfer Measurements in Free Flight at Mach Numbers up to 14.6 on a Flat-Faced Conical Nose With a Total Angle of 29°. NACA RM L57L03, 1958.

5. The Rocket Panel: Pressures, Densities, and Temperatures in the Upper Atmosphere. Phys. Rev., vol. 88, no. 5, Second ser., Dec. 1, 1952, pp. 1027-1032.

6. Hill, P. R.: A Method of Computing the Transient Temperature of Thick Walls From Arbitrary Variation of Adiabatic-Wall Temperature and Heat-Transfer Coefficient. NASA Rep. 1372, 1958. (Supersedes NACA TN 4105.)

7. Coulbert, C. D., MacInnes, W. F., Ishimoto, T., Bussell, B., and Ambrosio, A.: Temperature Response of Infinite Flat-Plates and Slabs to Heat Inputs of Short Duration at One Surface. Contract No. AF33(038)-1438), Dept. Eng., Univ. of California, Apr. 1951.

8. Fay, J. A., and Riddell, F. R.: Theory of Stagnation Point Heat Transfer in Dissociated Air. Jour. Aero. Sci., vol. 25, no. 2, Feb. 1958, pp. 73-85, 121.

9. Ames Research Staff: Equations, Tables, and Charts for Compressible Flow. NACA Rep. 1135, 1953. (Supersedes NACA TN 1428.)

10. Stoney, William E., Jr.: Aerodynamic Heating of Blunt Nose Shapes at Mach Numbers up to 14. NACA RM L58E05a, 1958.

11. Stoney, William E., Jr., and Markley, J. Thomas: Heat Transfer and Pressure Measurements on Flat-Faced Cylinders at Mach Number 2.0. NACA TN 4300, 1958.

[redacted]

[redacted]

12. Offenhartz, E., and Weisblatt, H.: Experimental Determination of the Turbulent Heat Transfer Rate Distribution Along the Forebody of Shape 52 From Shock Tube Experiments. RAD-TR-2-58-7 (Contract No. AF-04(645)-30), AVCO Res. and Advanced Dev. Div., June 16, 1958.

13. Lees, Lester: Laminar Heat Transfer Over Blunt-Nosed Bodies at Hypersonic Flight Speeds. Jet Propulsion, vol. 26, no. 4, Apr. 1956, pp. 259-269.

14. Stine, Howard A., and Wanlass, Kent: Theoretical and Experimental Investigation of Aerodynamic-Heating and Isothermal Heat-Transfer Parameters on a Hemispherical Nose With Laminar Boundary Layer at Supersonic Mach Numbers. NACA TN 3344, 1954.

15. Van Driest, E. R.: On Skin Friction and Heat Transfer Near the Stagnation Point. Rep. No. AL-2267, North American Aviation, Inc., Mar. 1, 1956.

16. Lee, Dorothy B., and Faget, Maxime A.: Charts Adapted From Van Driest's Turbulent Flat-Plate Theory for Determining Values of Turbulent Aerodynamic Friction and Heat-Transfer Coefficients. NACA TN 3811, 1956.

[redacted]

DECLASSIFIED

[redacted]

TABLE I.- OUTSIDE WALL TEMPERATURE T_w, °F

Time, sec	Outside wall temperature, °F, at station -												
	1	2_a	2_b	3	4	5_a	5_b	5_c	6	7	8_a	8_b	8_c
104.0	185	185	185	183	183	185	187	187	185	188	192	170	178
104.5	186	187	187	184	185	185	189	188	186	188	192	171	180
105.0	188	189	190	186	186	186	191	190	187	188	192	173	181
105.5	191	192	194	189	188	188	193	192	189	189	193	175	182
106.0	194	195	197	192	190	191	195	195	191	190	194	177	185
106.5	198	199	200	195	193	193	199	198	194	191	196	180	187
107.0	204	204	204	200	198	196	204	203	198	195	199	186	191
107.5	210	211	211	206	202	201	212	211	203	198	204	192	195
108.0	219	218	223	217	209	207	224	223	211	204	213	199	203
108.5	231	227	238	233	221	219	237	235	224	213	227	206	216
109.0	248	244	254	250	239	234	251	250	240	226	240	217	230
109.2	255	253	260	257	246	240	257	257	246	232	246	223	235
109.4	263	262	266	264	254	247	263	265	253	237	253	228	241
109.6	271	272	273	272	262	254	270	274	261	243	261	234	247
109.8	279	282	281	281	269	261	277	283	268	249	269	241	253
110.0	289	291	289	291	277	268	285	293	278	255	278	248	260
110.2	299	302	297	301	286	276	295	303	288	263	288	255	268
110.4	311	314	306	313	294	284	307	313	299	271	298	263	276
110.6	326	326	318	328	302	295	320	324	313	280	309	272	285
110.8	342	341	336	344	312	309	336	337	329	290	322	280	296
111.0	362	358	359	363	324	325	354	354	347	302	336	291	309
111.2	385	380	384	385	339	343	376	376	368	316	352	303	325
111.4	412	406	410	413	360	364	402	403	392	333	371	318	343
111.6	449	439	437	449	384	389	431	438	422	351	393	336	364
111.8	494	483	465	495	417	418	467	478	462	372	418	357	389
112.0	545	544	501	552	458	454	514	525	511	394	445	378	415
112.2	602	612	546	616	506	496	572	577	569	417	476	403	444
112.4	667	684	601	682	557	545	634	634	628	441	510	432	474
112.6	742	759	---	754	612	598	696	696	689	466	547	---	---
112.8	824	834	---	826	668	656	757	760	750	492	585	---	---
112.9	868	871	---	863	696	686	788	794	781	505	605	---	---
113.0	---	---	---	---	---	---	818	---	---	---	---	---	---

[redacted]

[redacted]

[redacted]

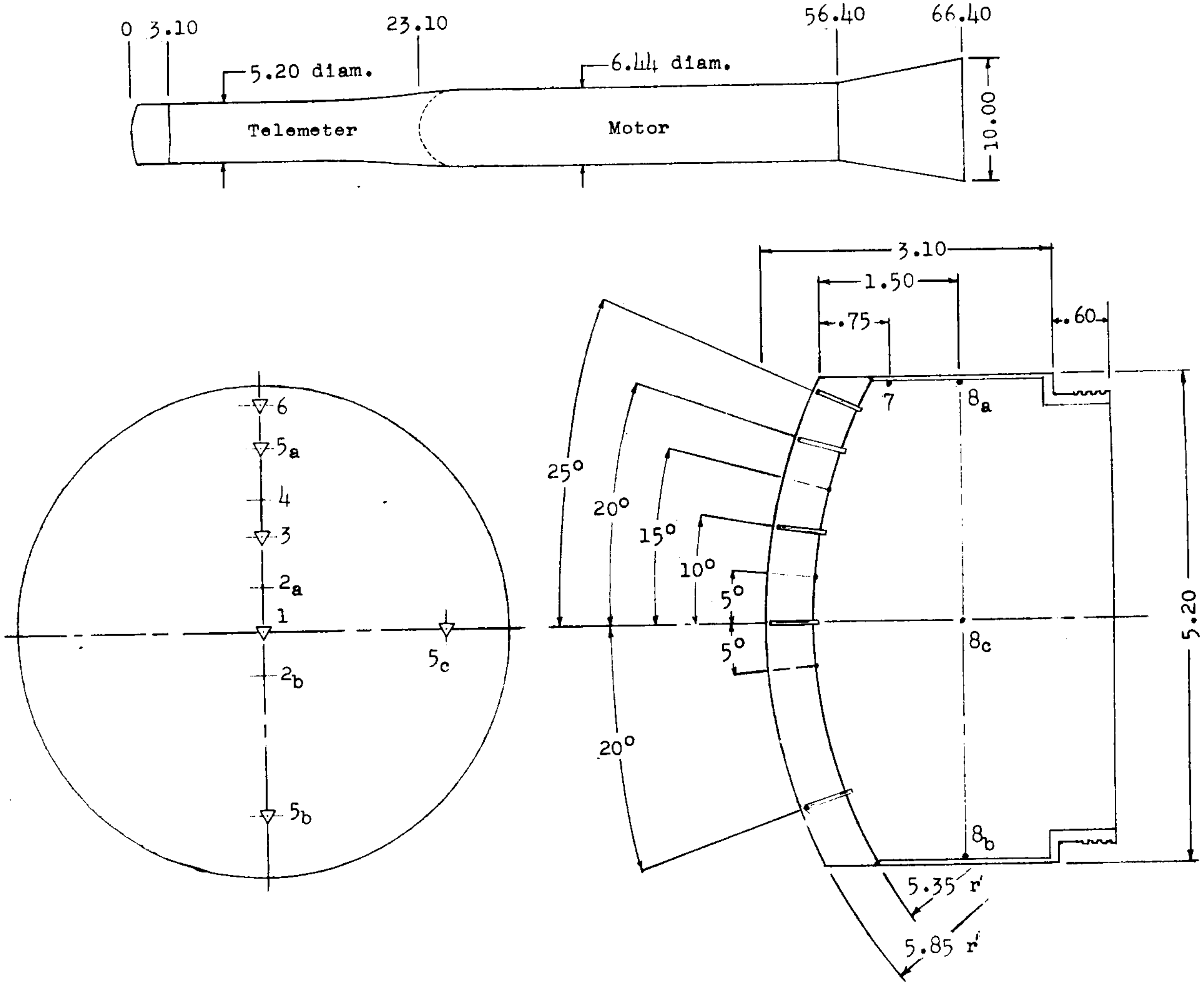

(a) Sketch of model and nose detail.

Figure 1.- Test nose. Dimensions are in inches.

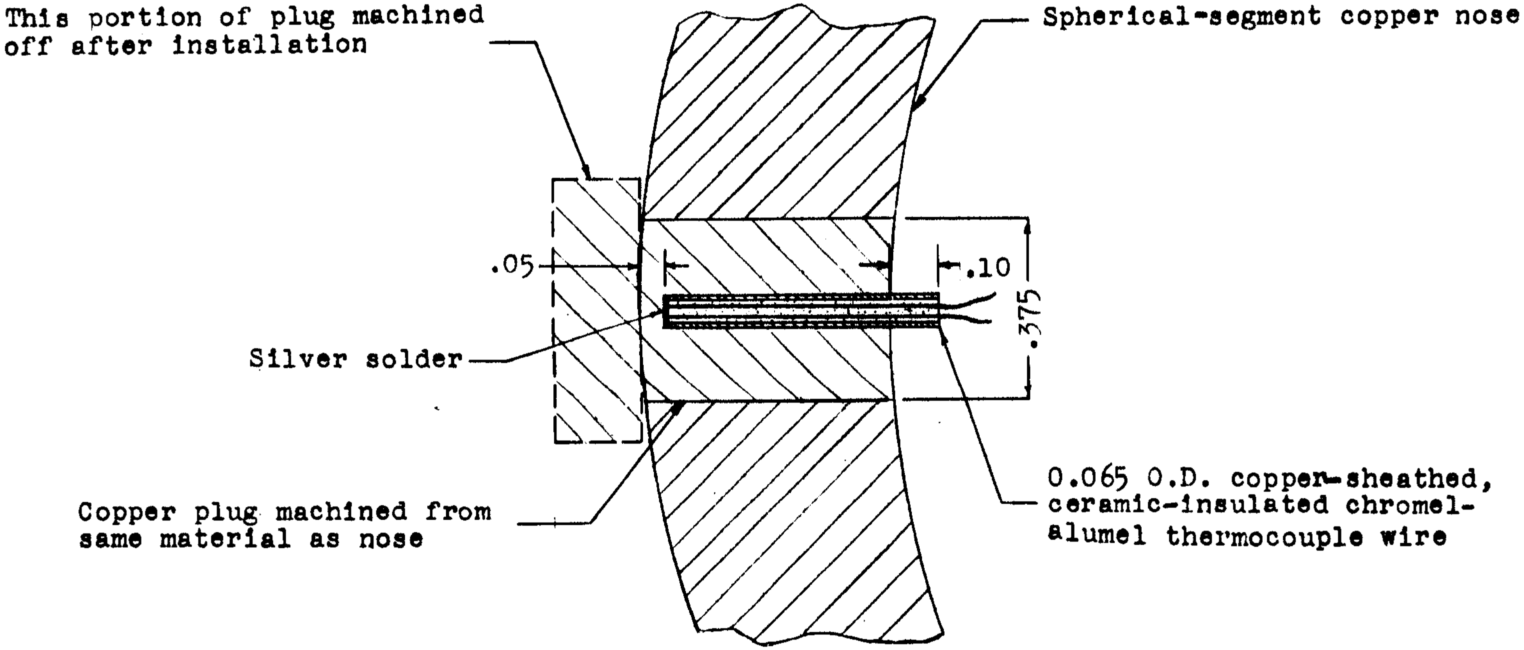

(b) Plug type of thermocouple installation.

Figure 1.- Concluded.

[redacted]

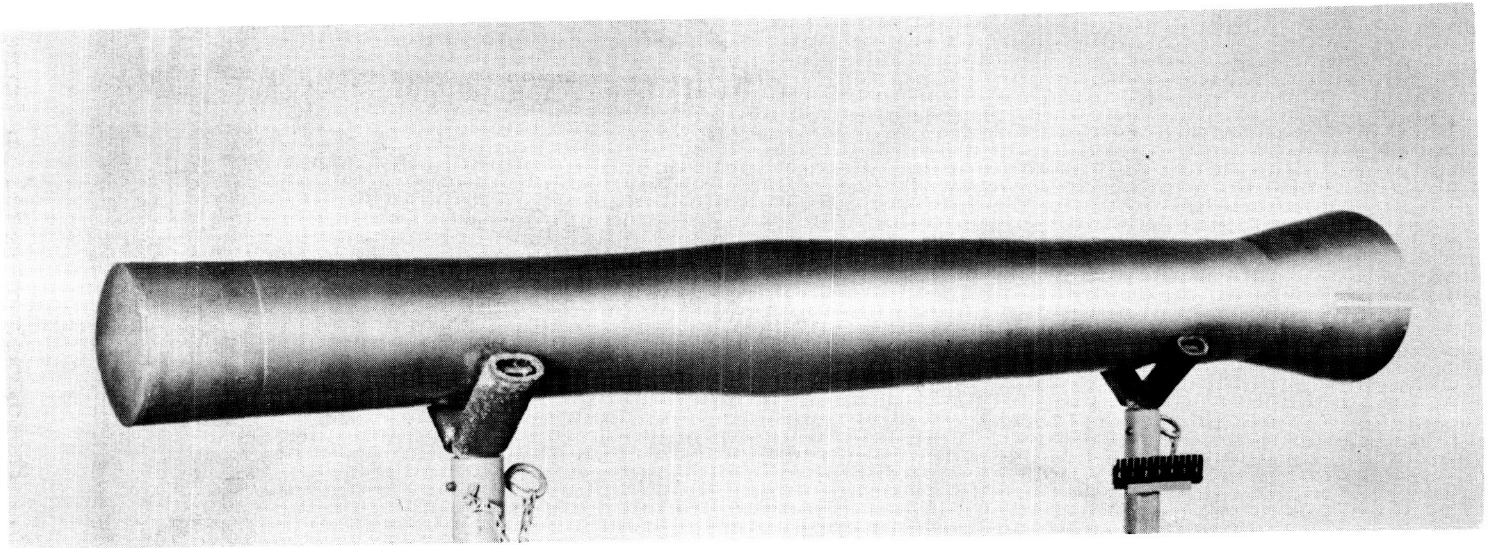

Figure 2.- Photograph of the model. L-58-2740

[redacted]

DECLASSIFIED [redacted]

L-617

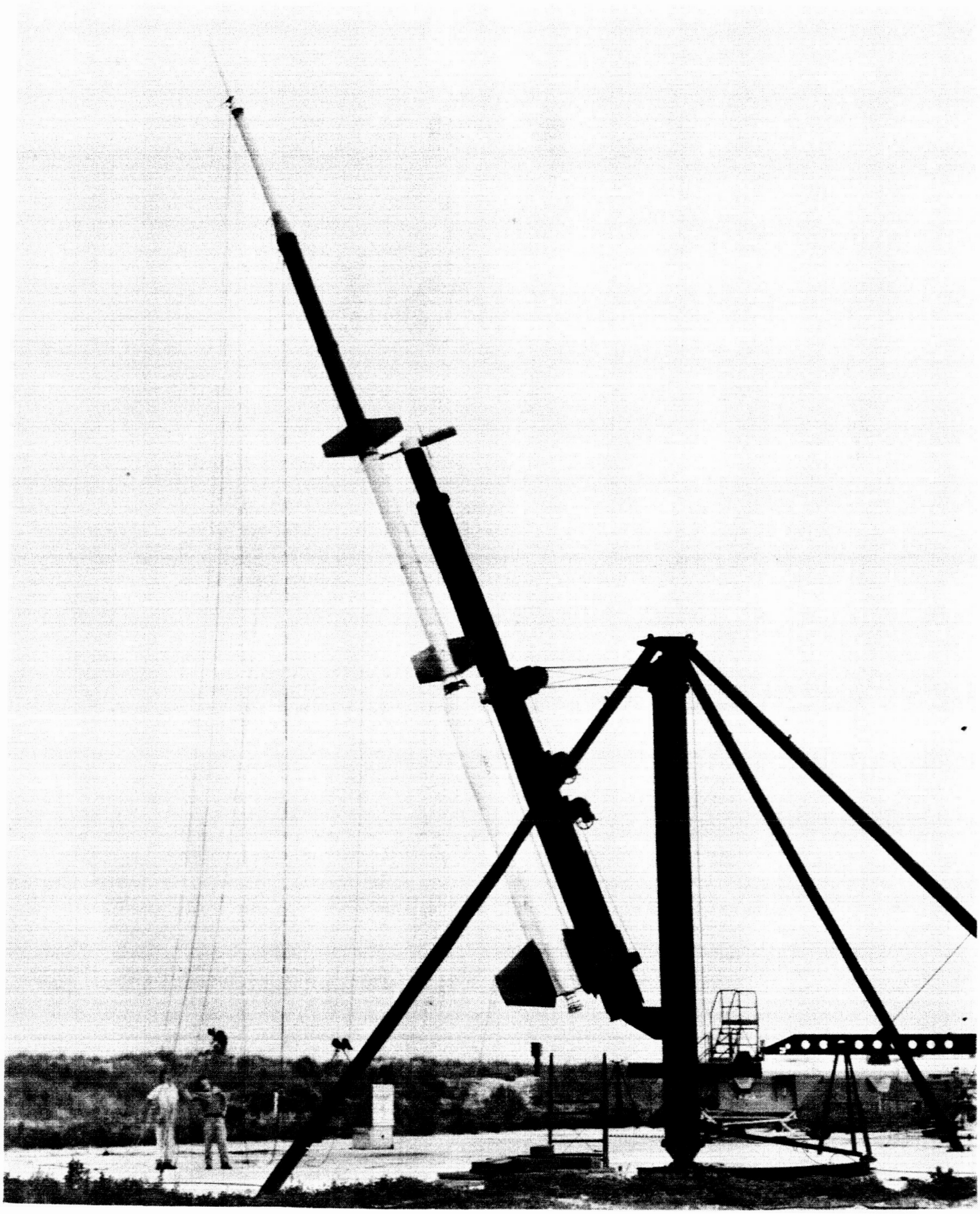

Figure 3.- Photograph of model on launcher. L-58-3016

[redacted]

[redacted]

[redacted]

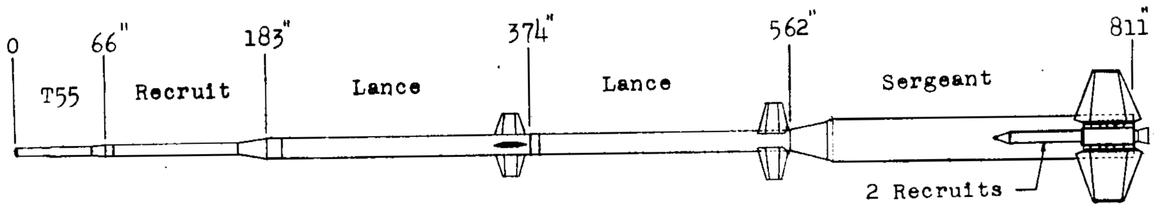

Stage	Motor designation	Loaded motor weight, lb	Propellant weight, lb	Stage weight, lb	Combination weight, lb	Average thrust, lb (a)	Nominal burning time, sec (a)
1	Two Recruits Sergeant	352 each 8185	265 each 7033	9588	13,727	32,000 each 50,000	1.6 27.5
2	**Lance** XM25	1730	1232	1820	4139	45,000	4.9
3	**Lance** XM25	1730	1232	1842	2319	45,000	4.9
4	**Recruit** XM19	352	265	393	477	32,000	1.6
5	T55	40	33.6	84	84	4650	1.4

[a] From manufacturer's specifications.

Figure 4.- Complete configuration and table of motor characteristics.

DECLASSIFIED

[redacted]

L-617

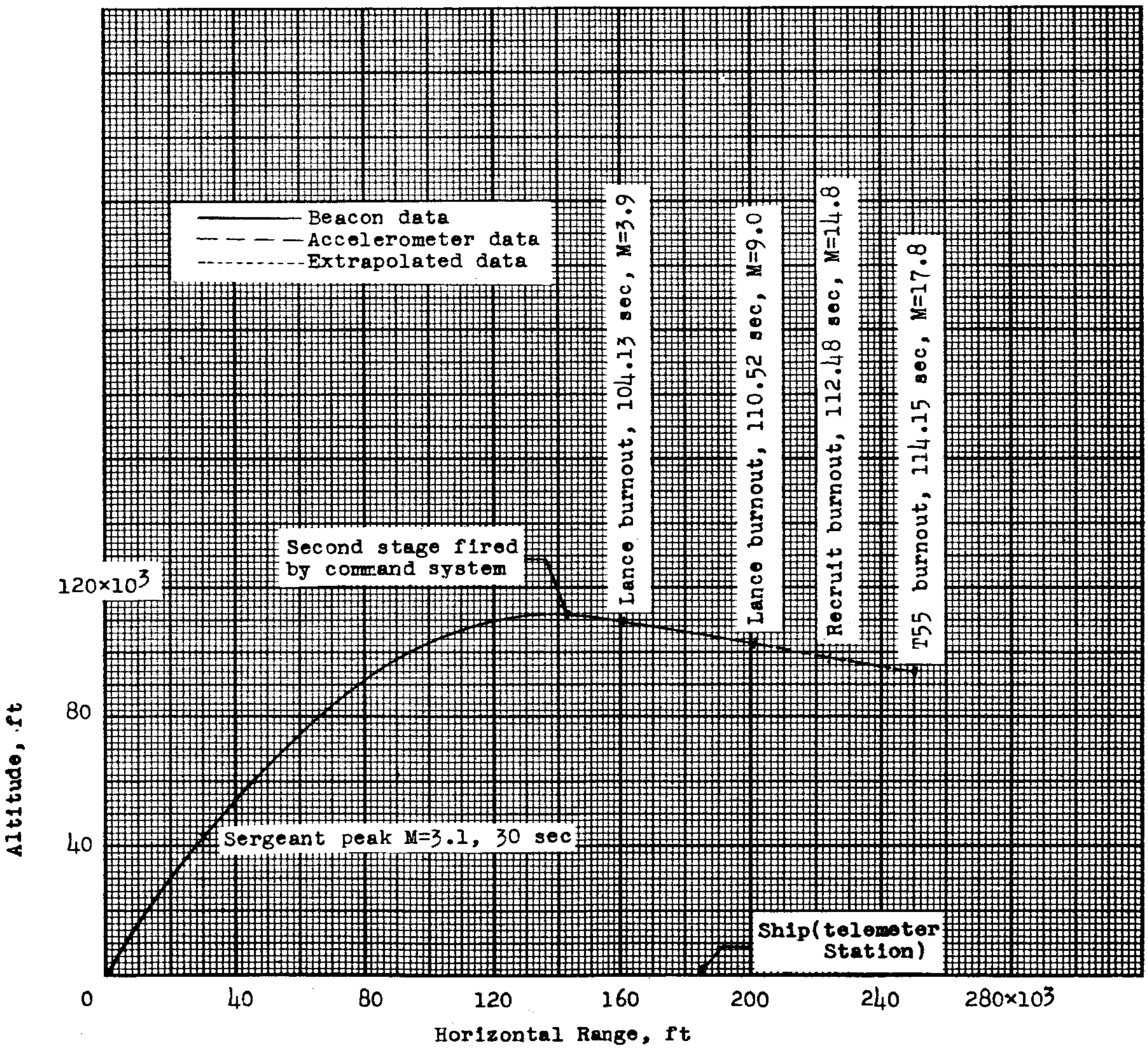

Figure 5.- Flight trajectory.

[redacted]

[redacted]

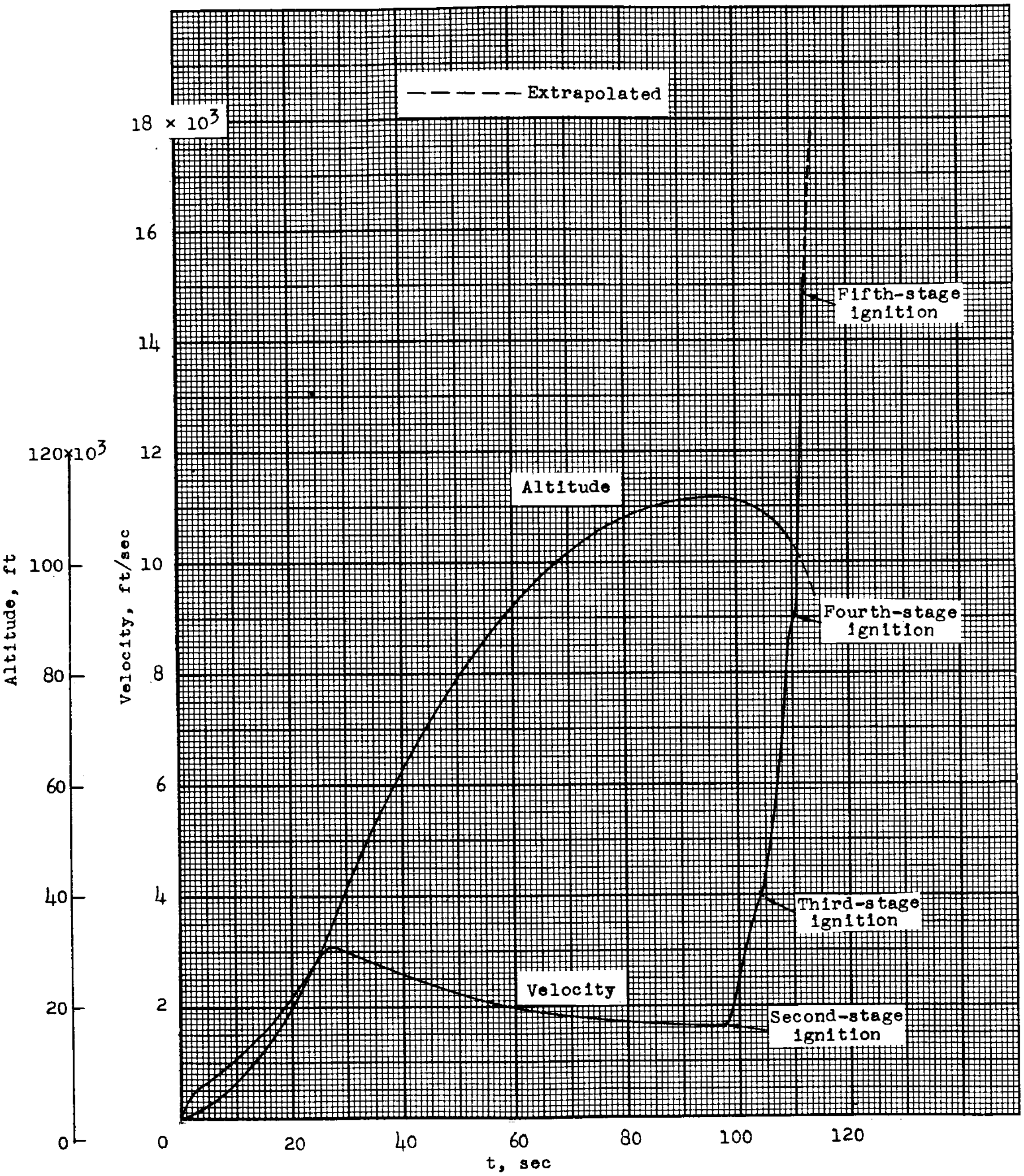

(a) Velocity and altitude.

Figure 6.- Time histories of flight conditions.

[redacted]

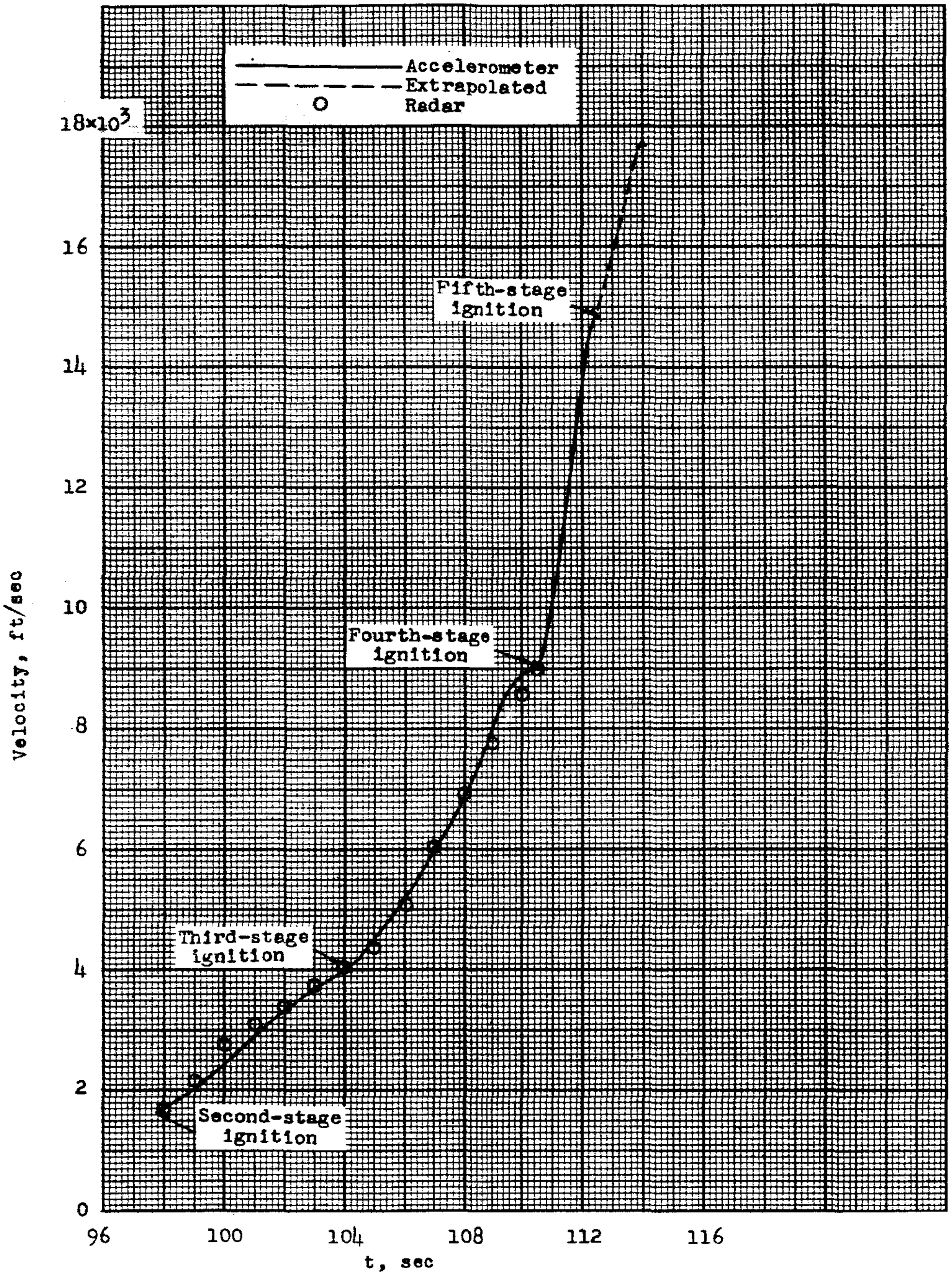

(b) Comparison between radar and accelerometer velocities.

Figure 6.- Continued.

[redacted]

[redacted]

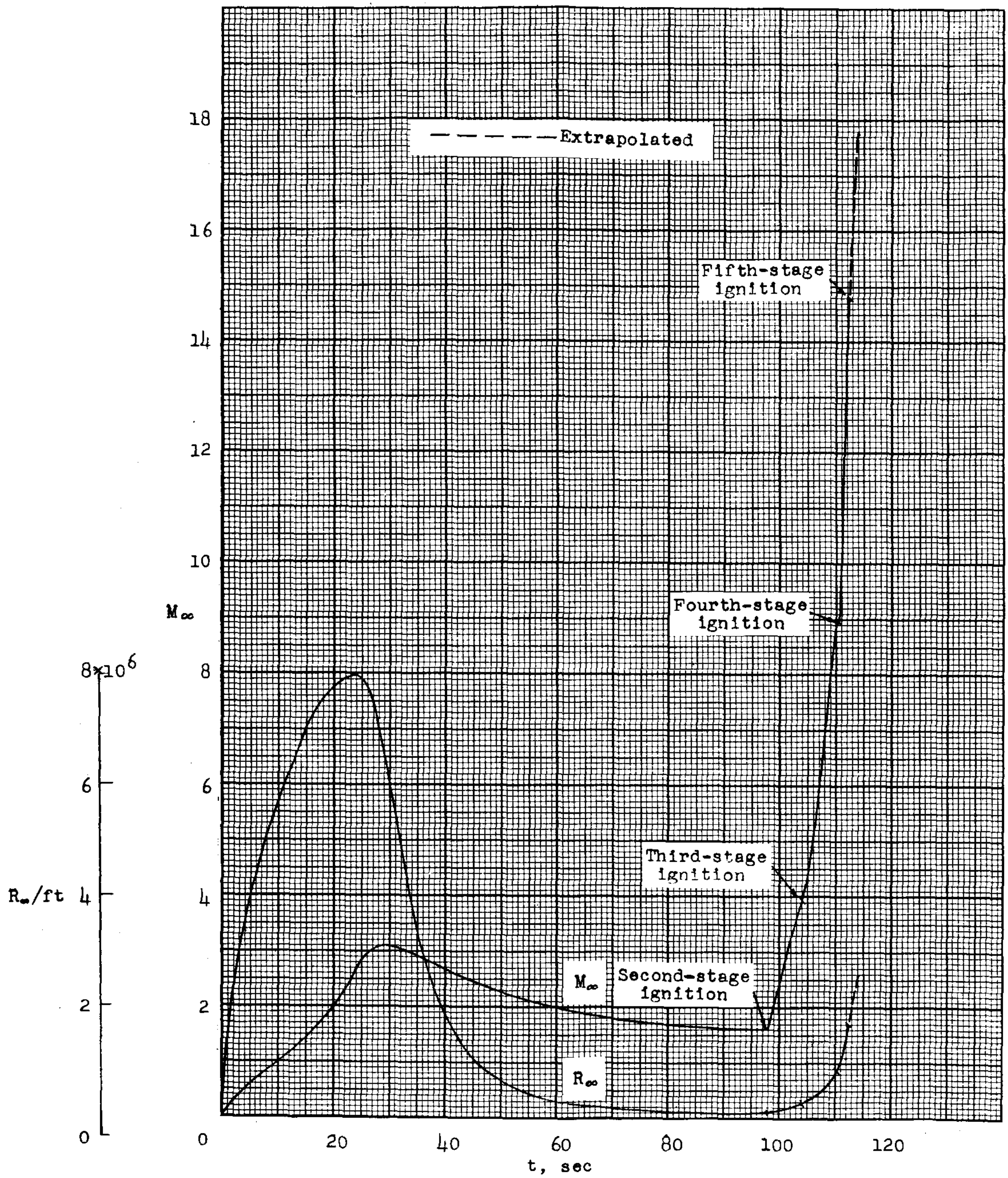

(c) Mach number and Reynolds number per foot.

Figure 6.- Concluded.

L-617

[redacted]

[redacted]

[redacted]

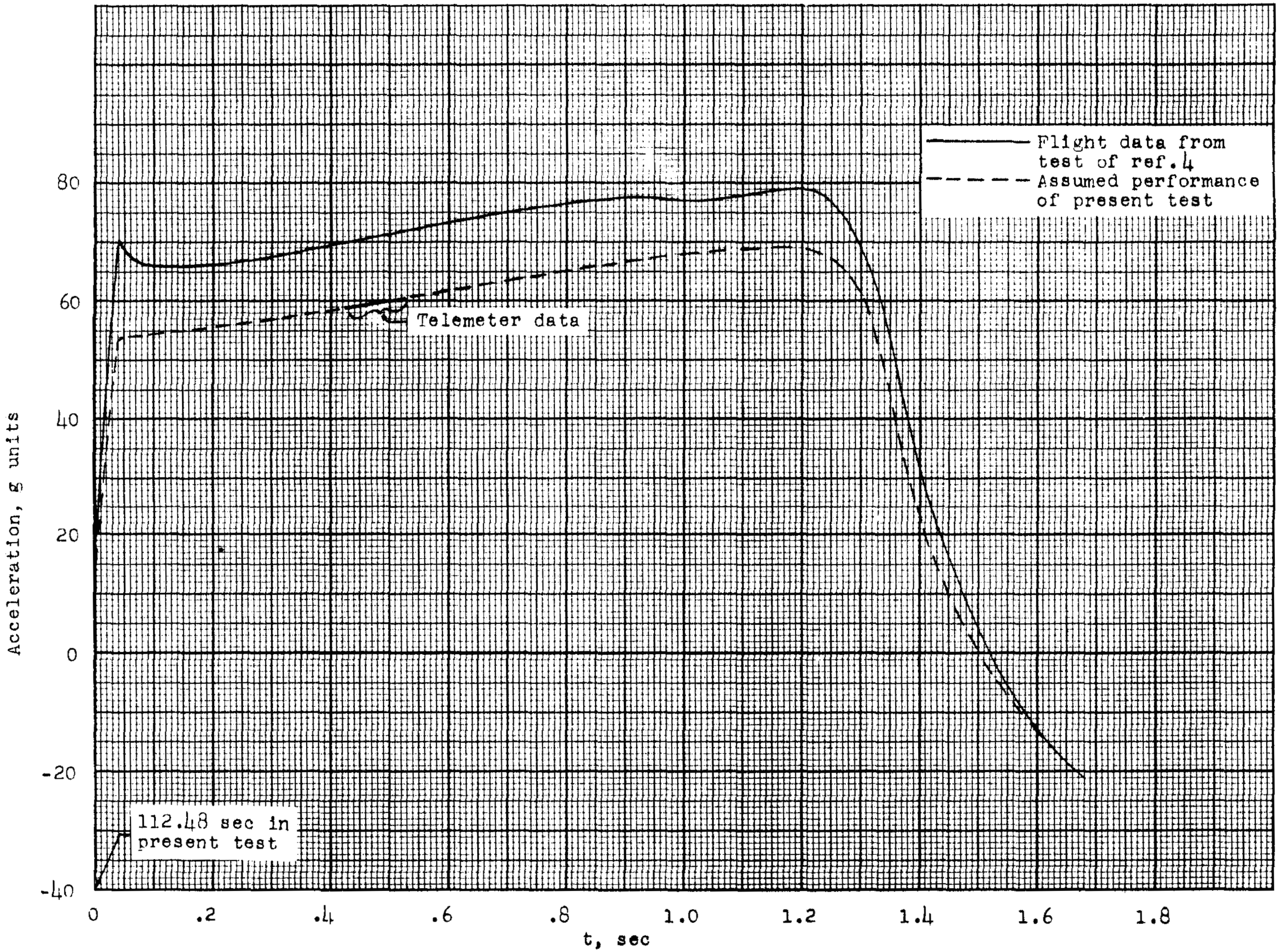

Figure 7.- Accelerometer data during fifth-stage burning.

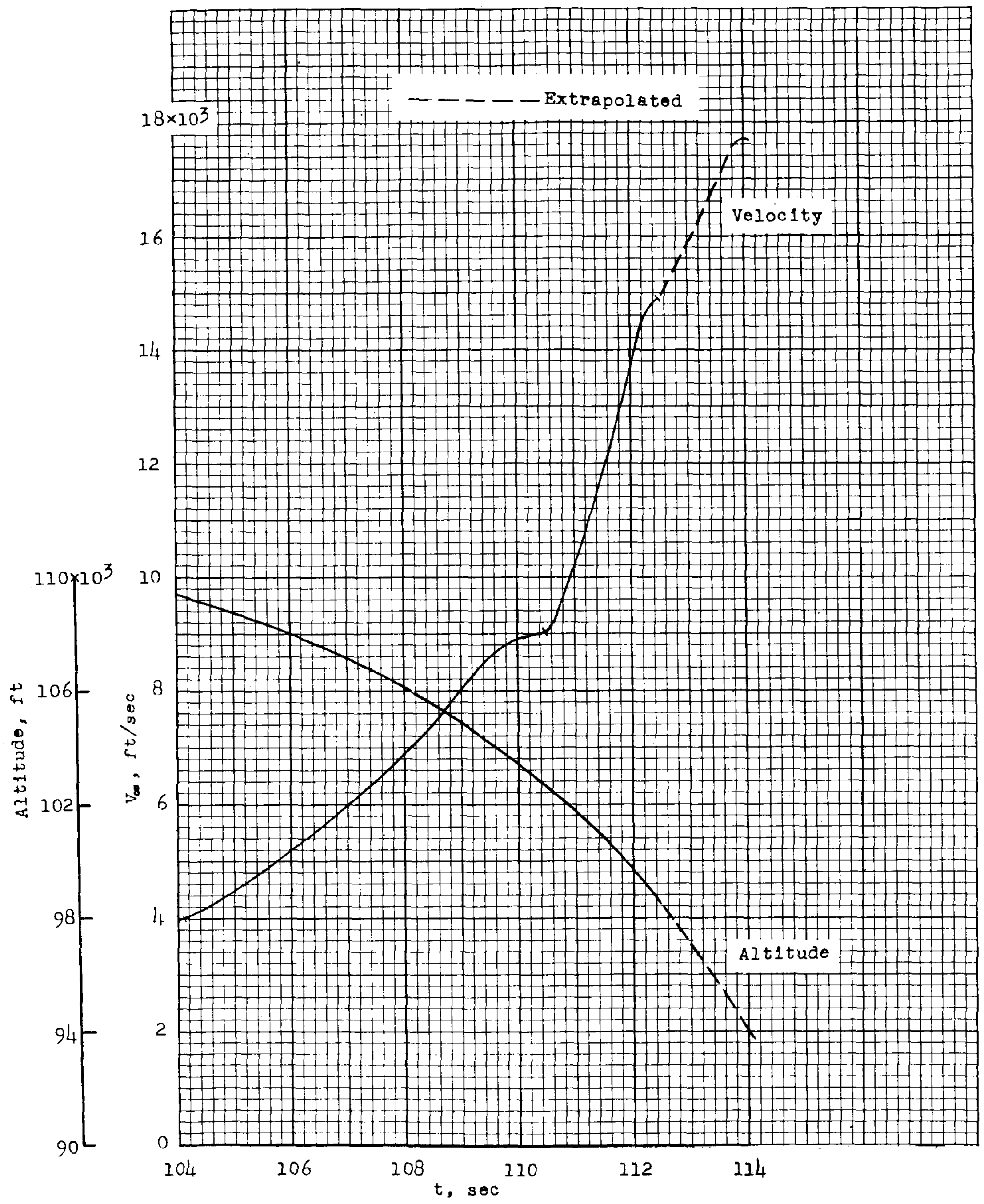

(a) Velocity and altitude.

Figure 8.- Time histories of flight conditions during high-speed portion of test.

[redacted]

[redacted]

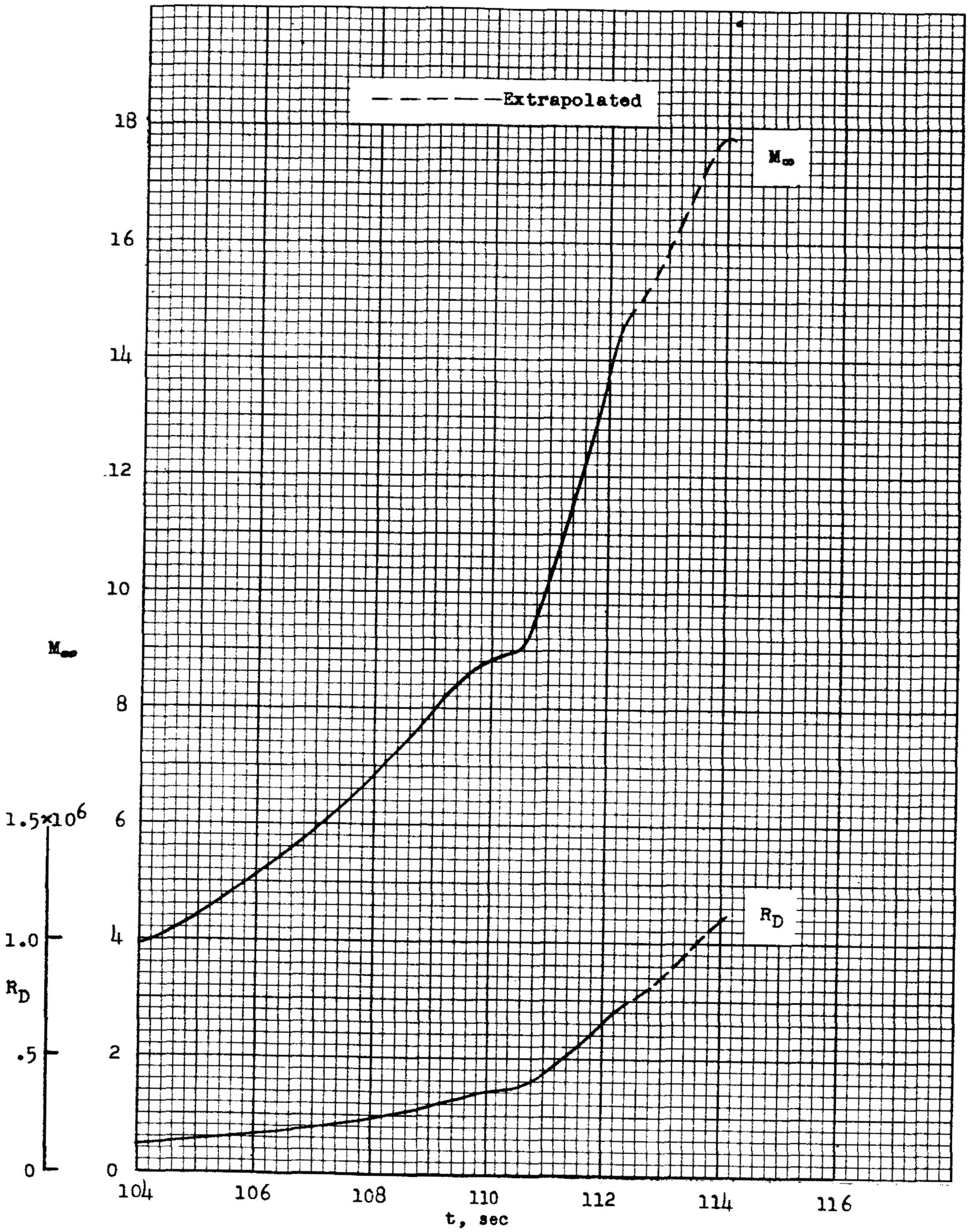

(b) Mach number and Reynolds number based on nose diameter.

Figure 8.- Concluded.

[redacted]

[redacted]

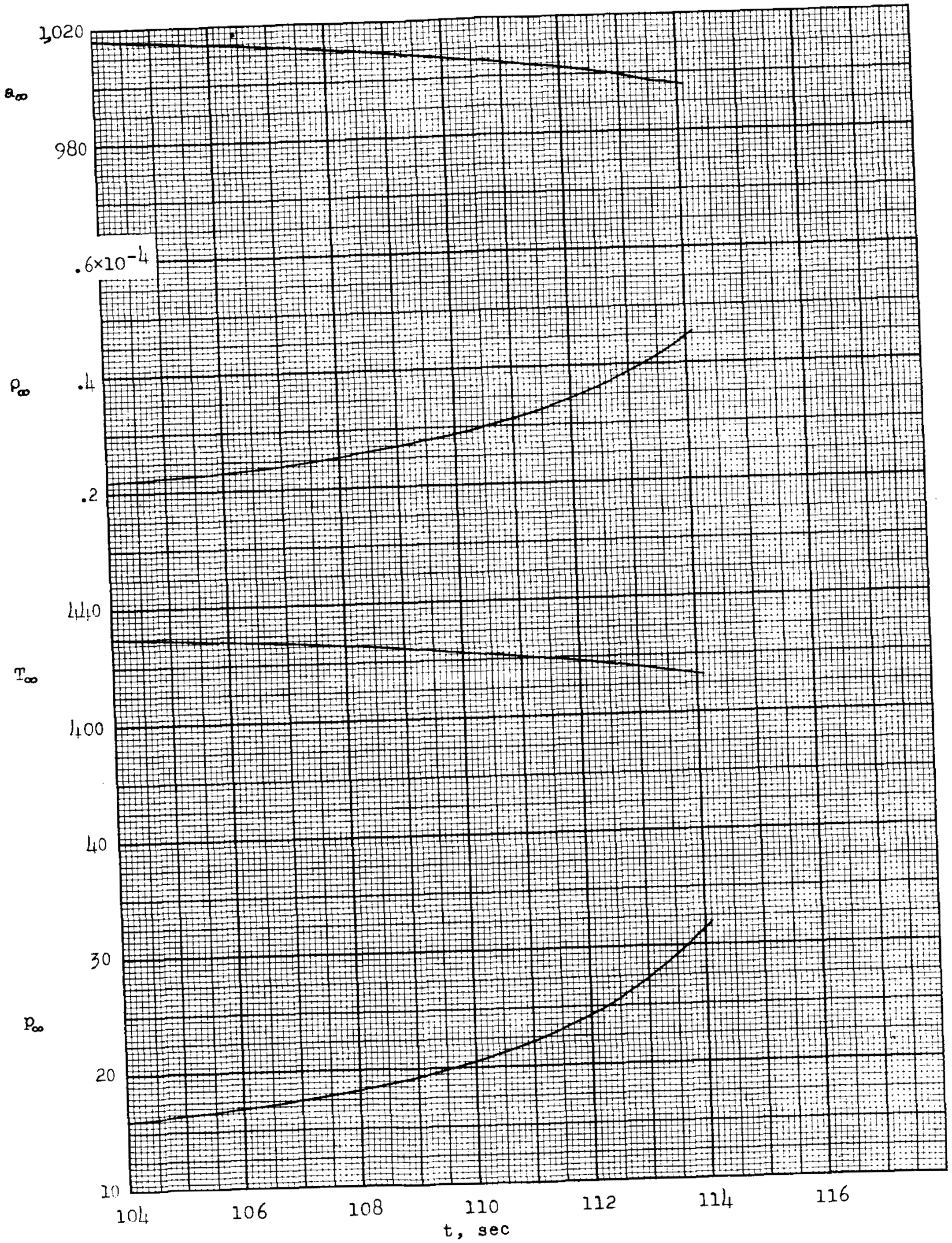

Figure 9.- Ambient conditions (standard atmosphere) for high-speed portion of test.

[redacted]

[redacted]

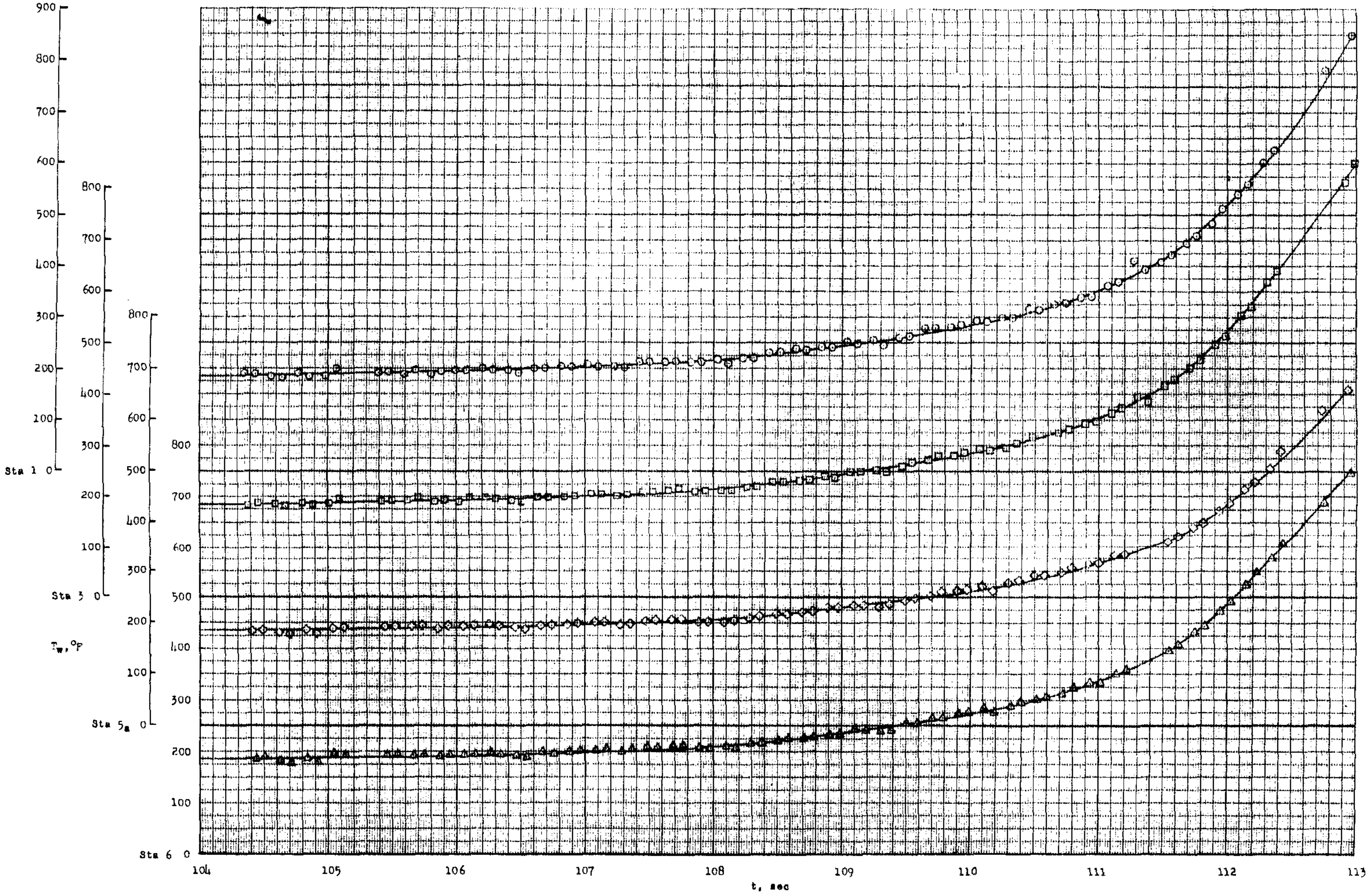

(a) Temperatures measured by plug type of thermocouples. Stations 1, 3, 5_a, and 6.

Figure 10.- Time histories of typical skin temperatures.

[redacted]

[redacted]

[redacted]

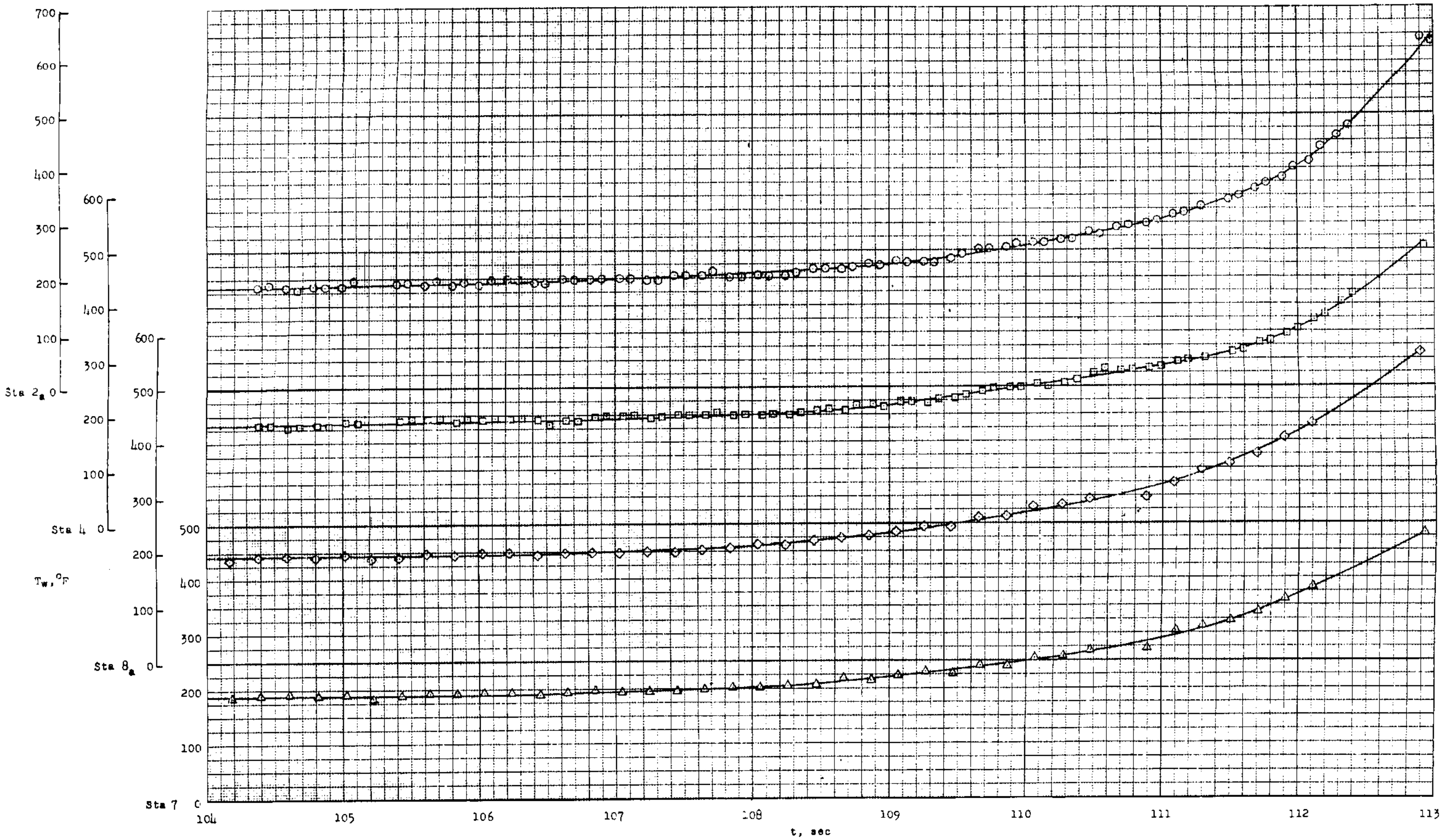

(b) Temperatures measured by peened and spot-welded thermocouples. Stations 2_a, 4, 7, and 8_a.

Figure 10.- Concluded.

[redacted]

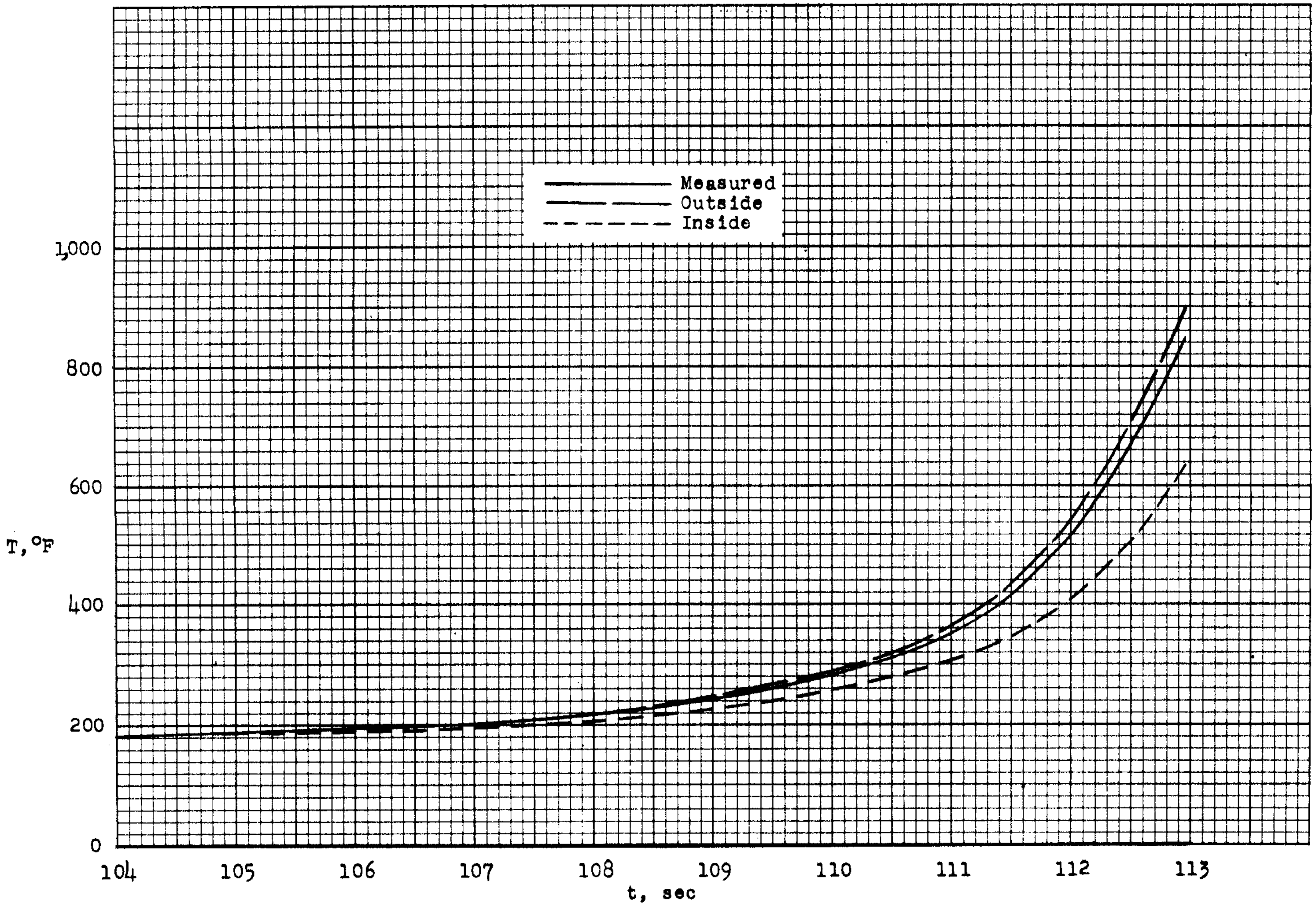

(a) Station 1.

Figure 11.- Time histories of typical outside, measured, and inside skin temperatures.

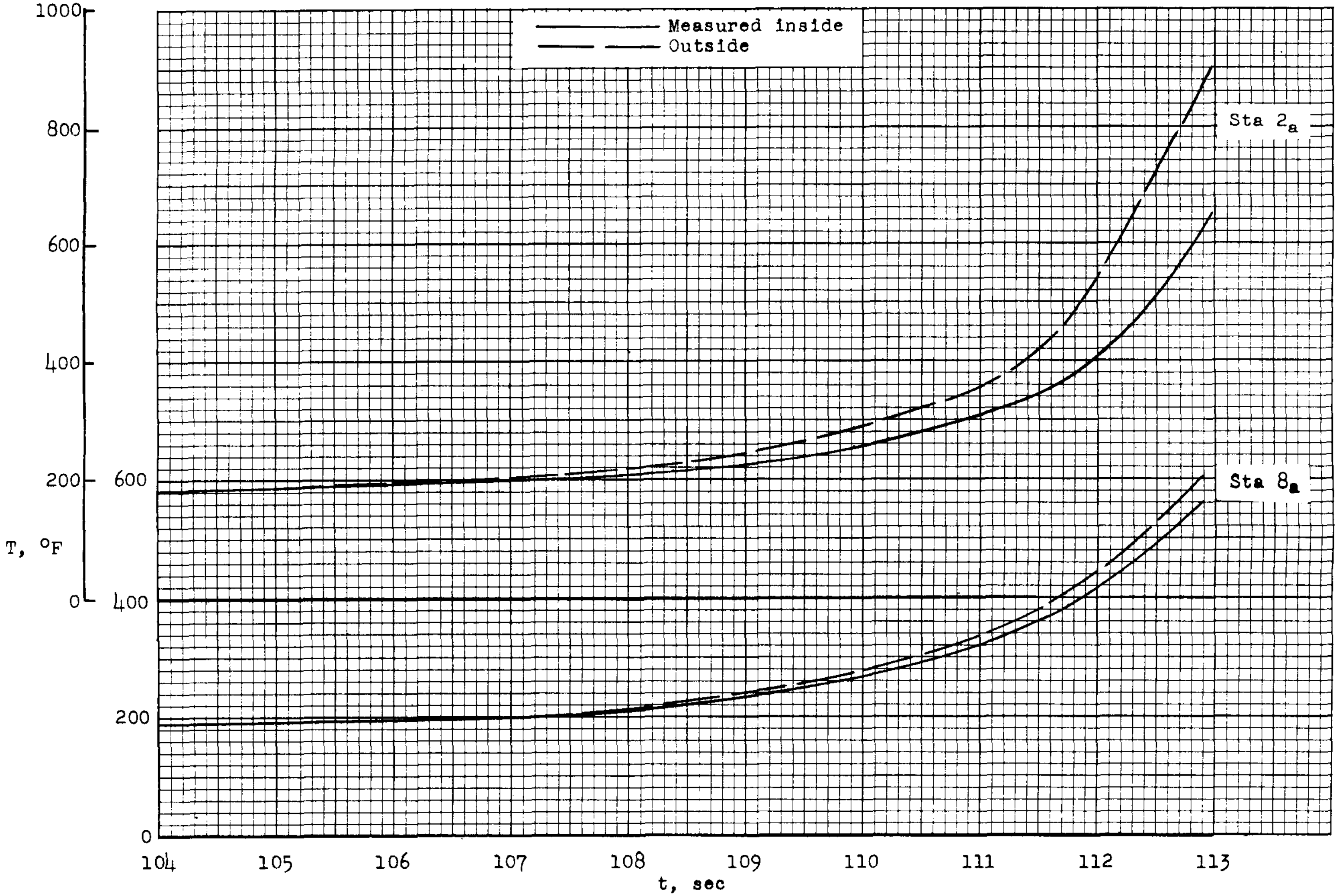

(b) Stations 2_a and 8_a.

Figure 11.- Concluded.

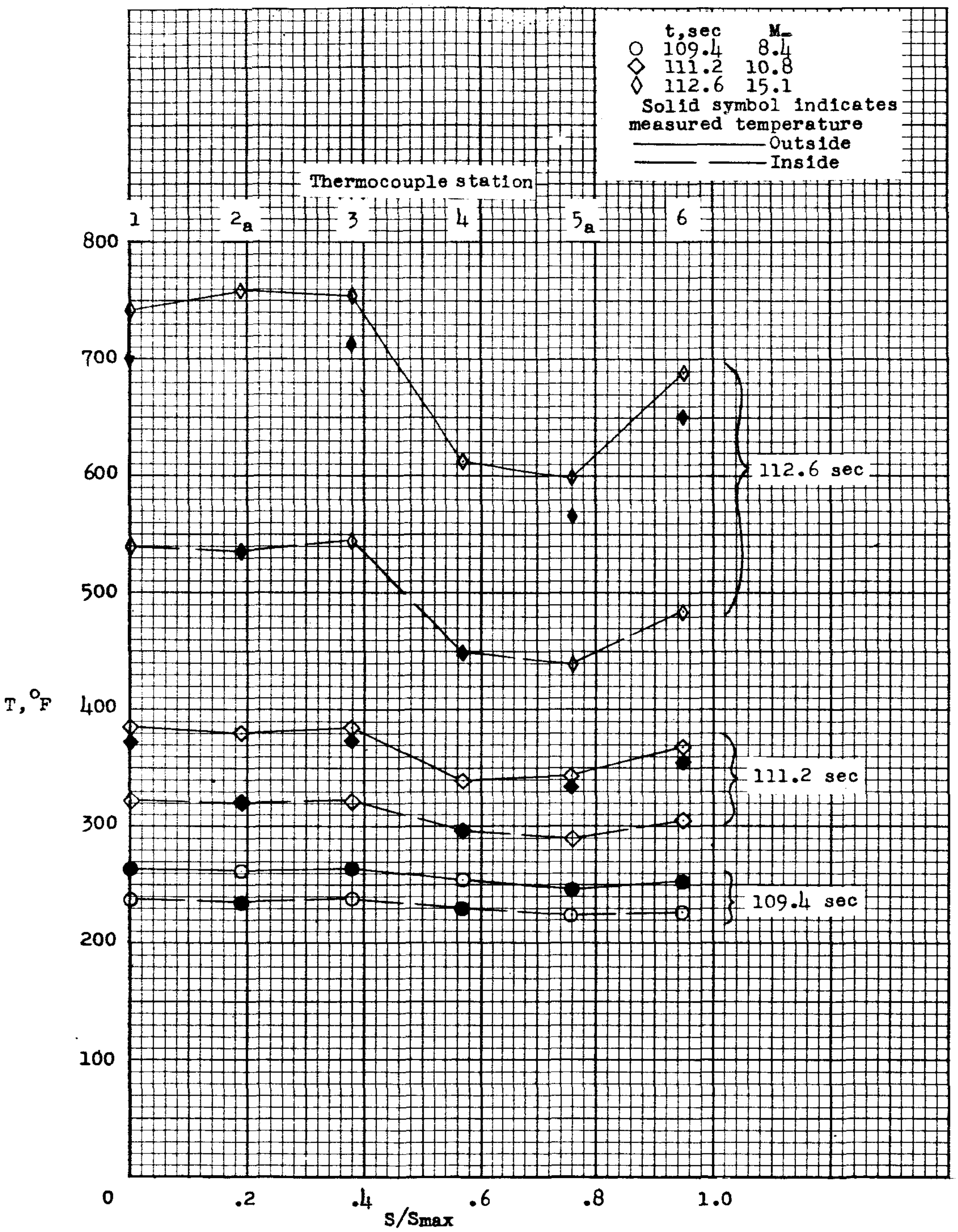

(a) Outside and inside wall temperatures.

Figure 12.- Distribution of wall temperature along nose surface.

[redacted]

L-617

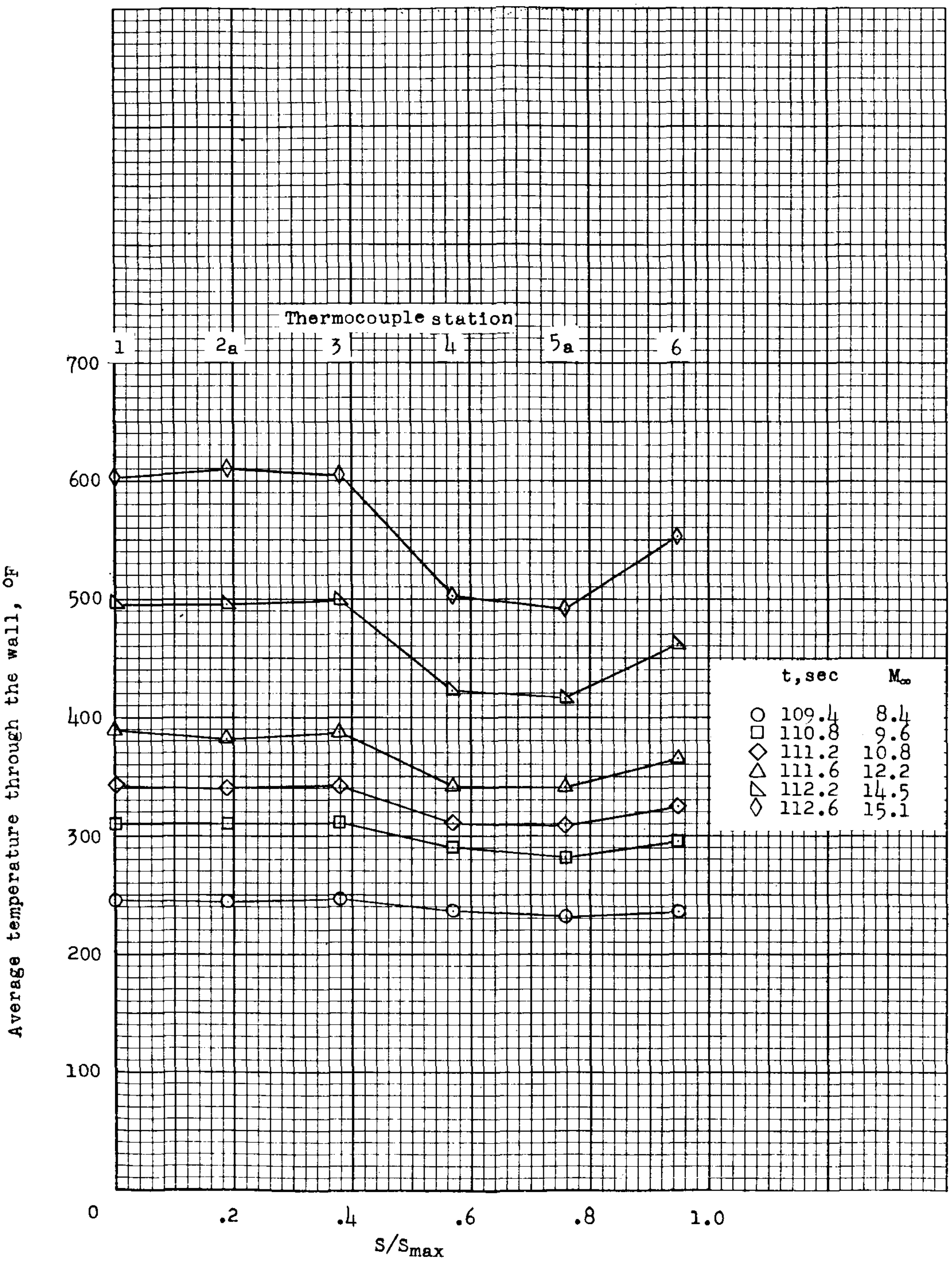

(b) Average wall temperature.

Figure 12.- Concluded.

[redacted]

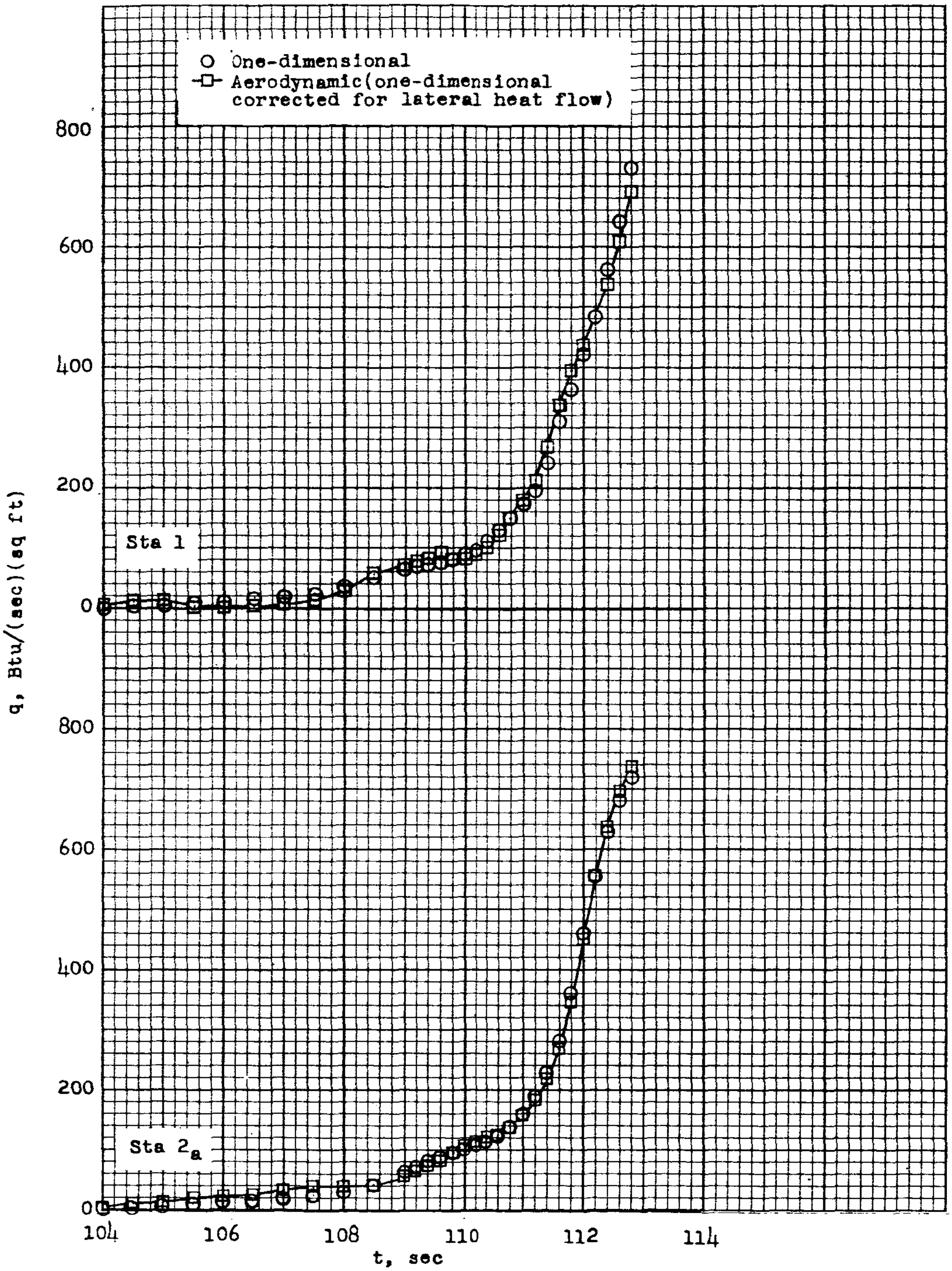

(a) Stations 1 and 2_a.

Figure 13.- Experimental heat-transfer data on spherical segment.

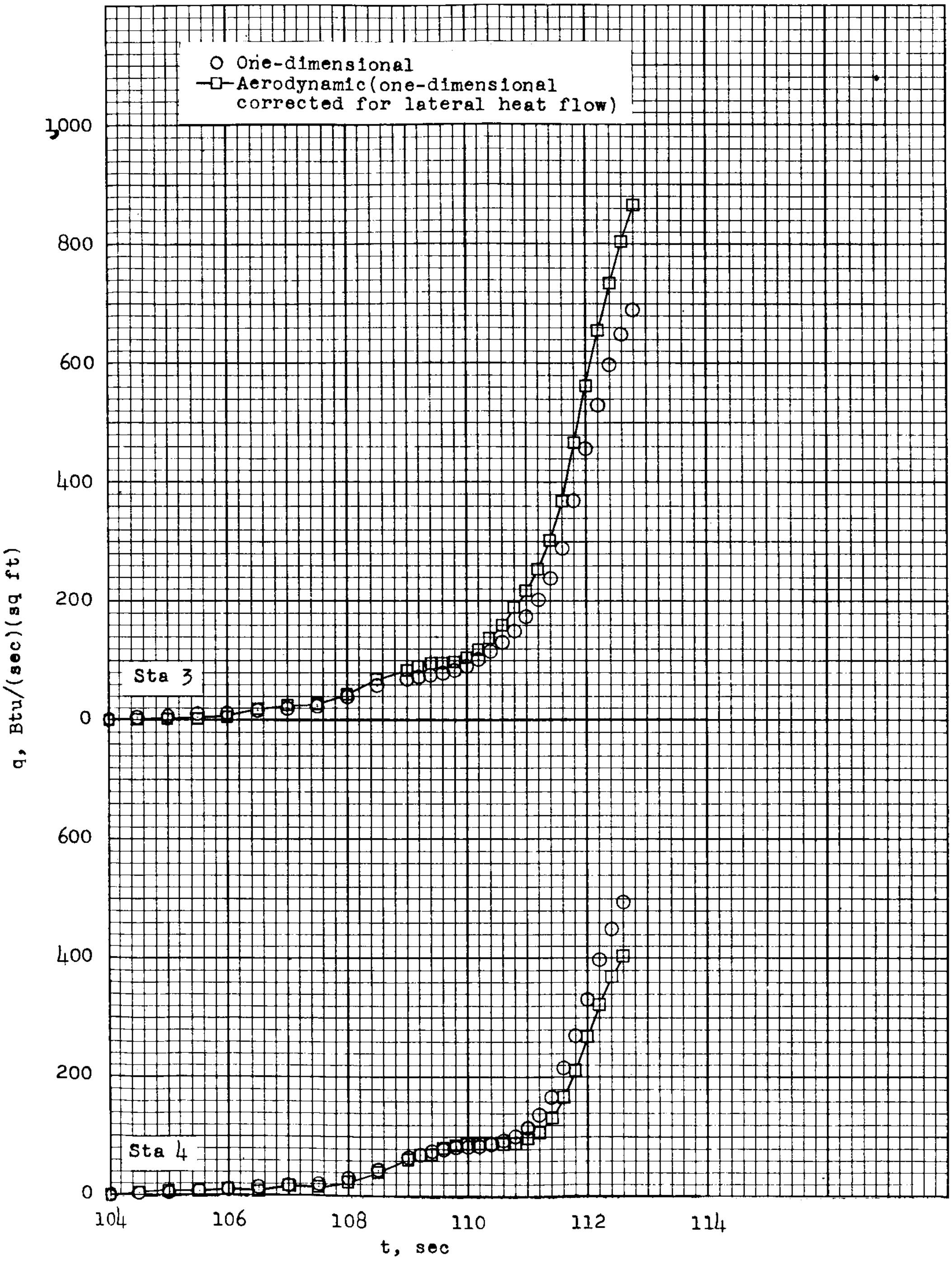

L-617

(b) Stations 3 and 4.

Figure 13.- Continued.

[redacted]

L-617

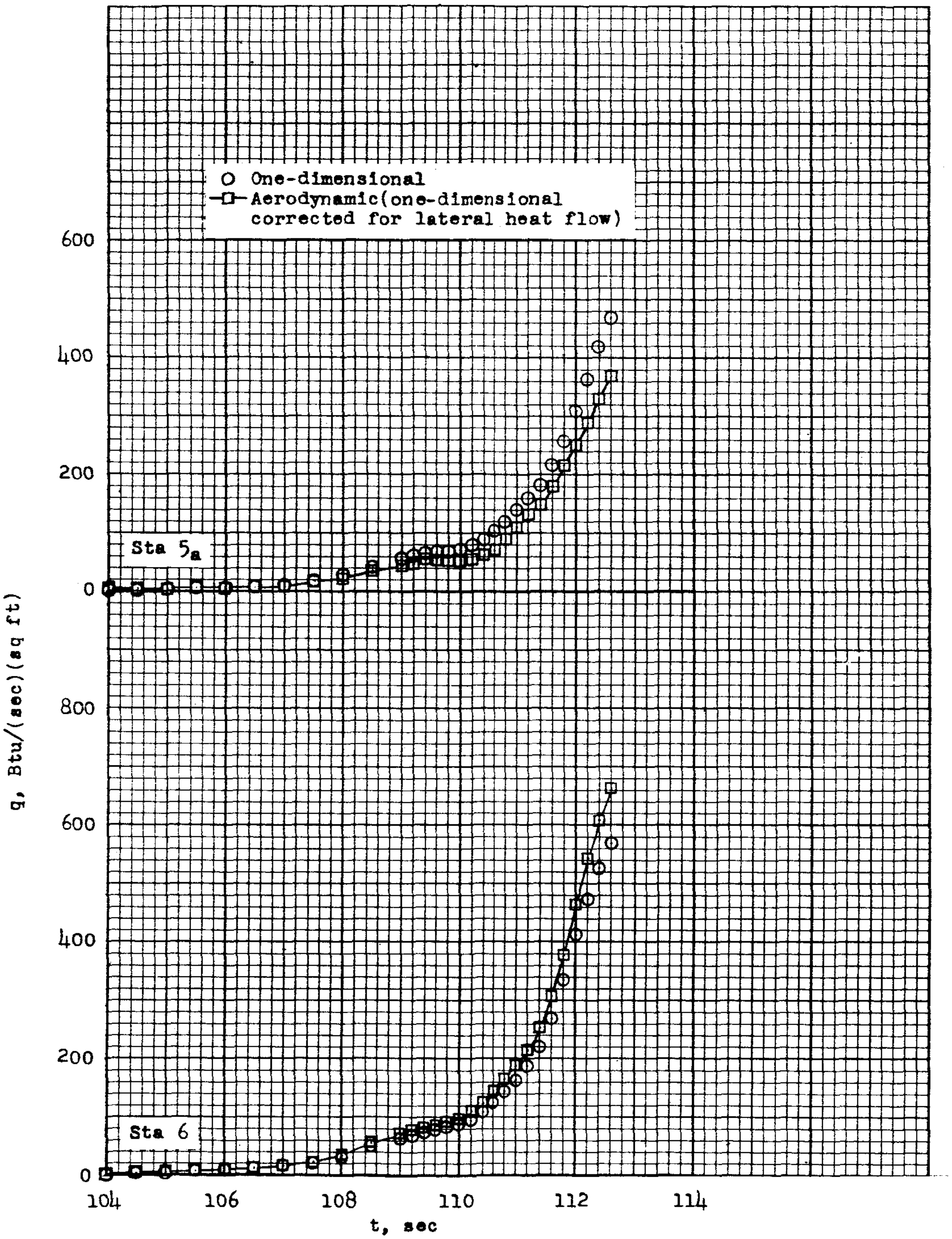

(c) Stations 5_a and 6.

Figure 13.- Concluded.

[redacted]

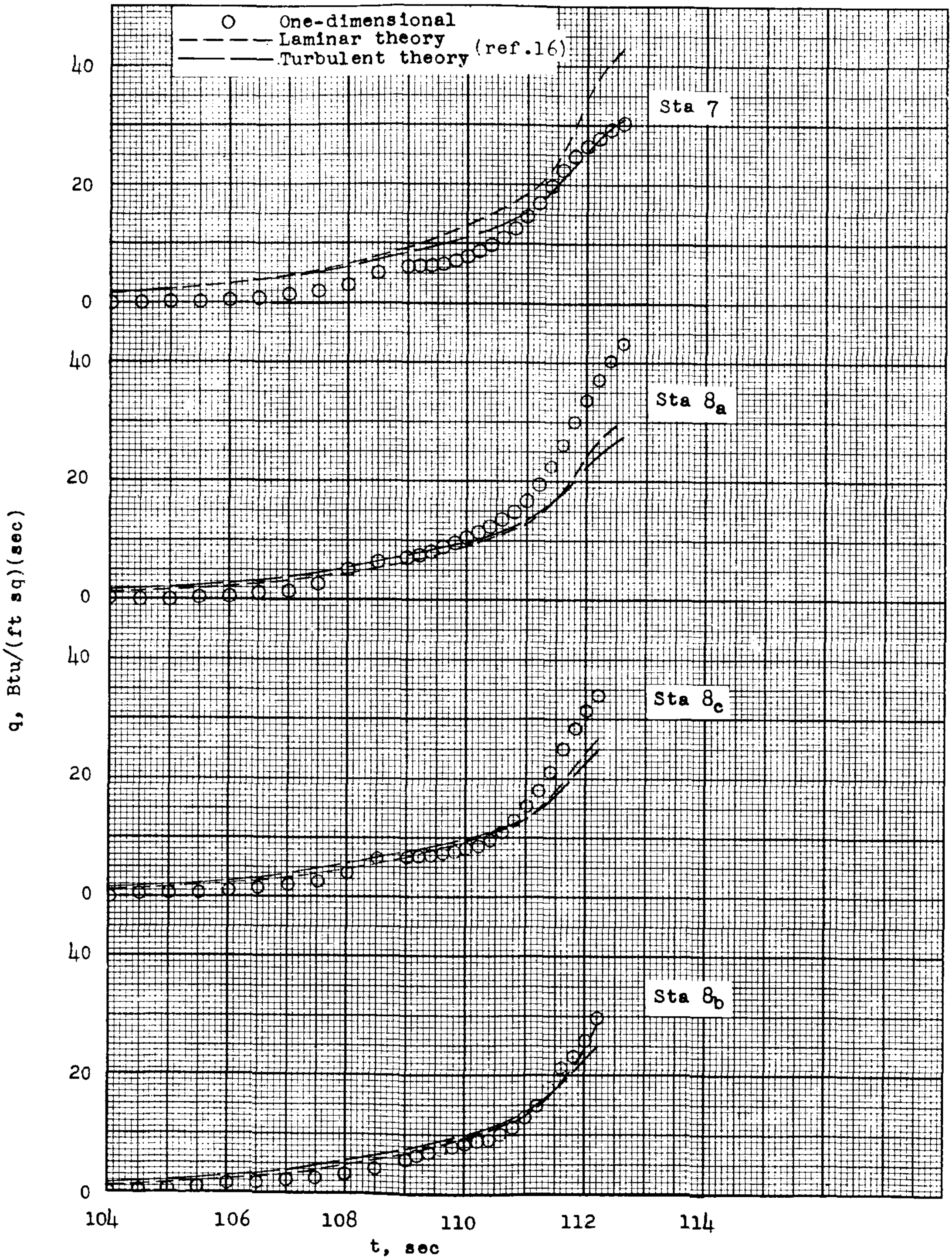

Figure 14.- Experimental and theoretical heating rates on cylinder of nose.

[redacted]

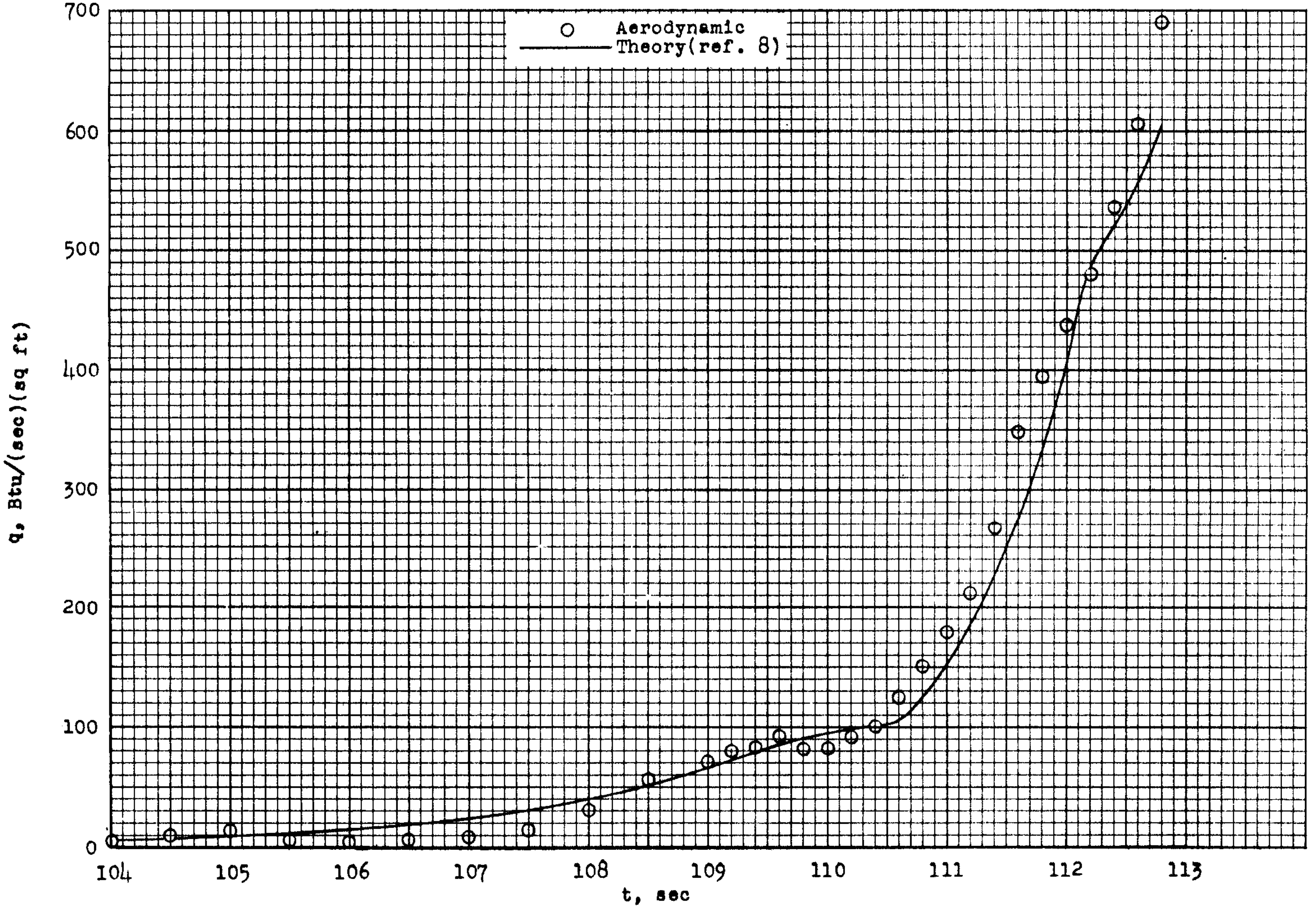

Figure 15.- Experimental and theoretical stagnation-point heating.

[redacted]

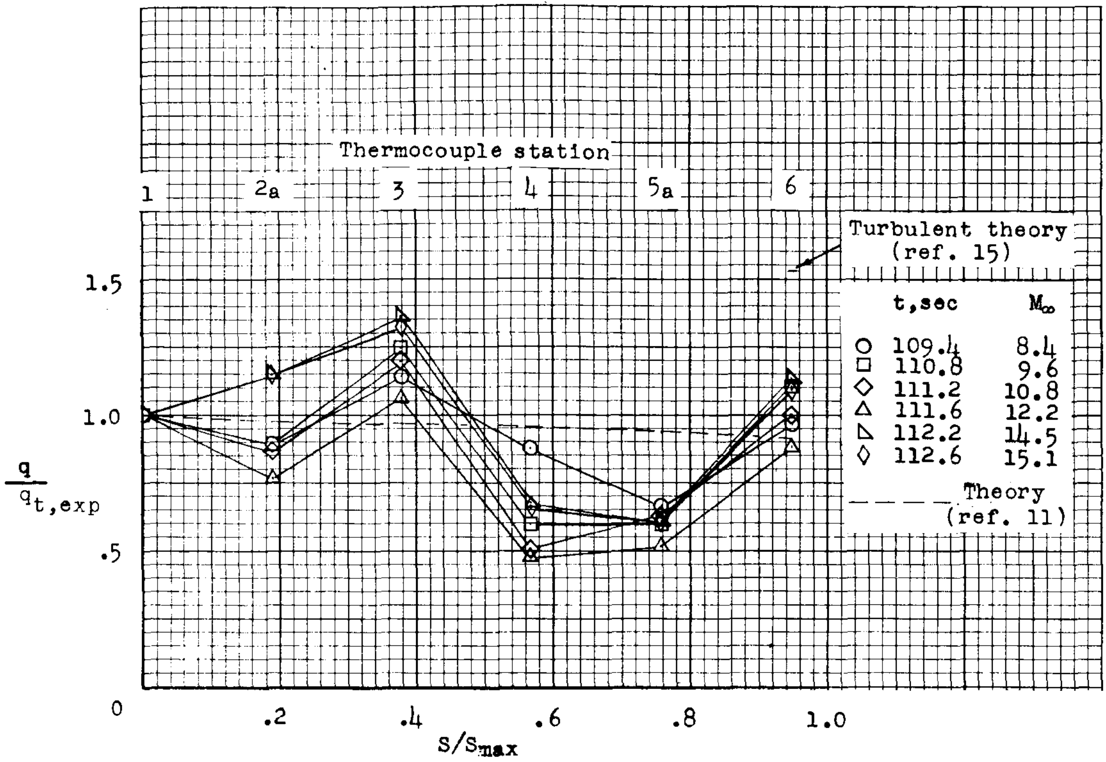

(a) Aerodynamic heating rates.

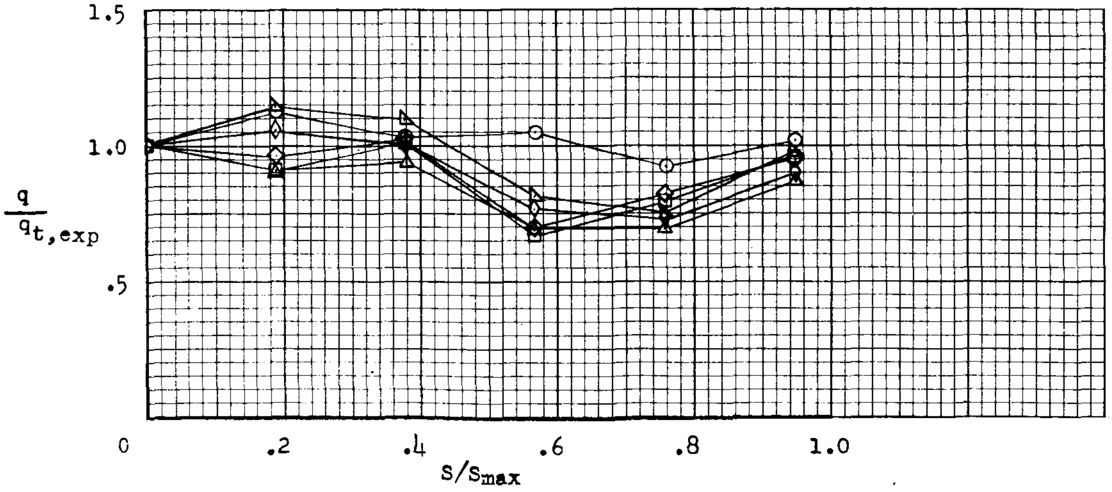

(b) One-dimensional heating rates.

Figure 16.- Distribution of experimental local heating rates on spherical-segment nose divided by stagnation-point values.

[redacted]

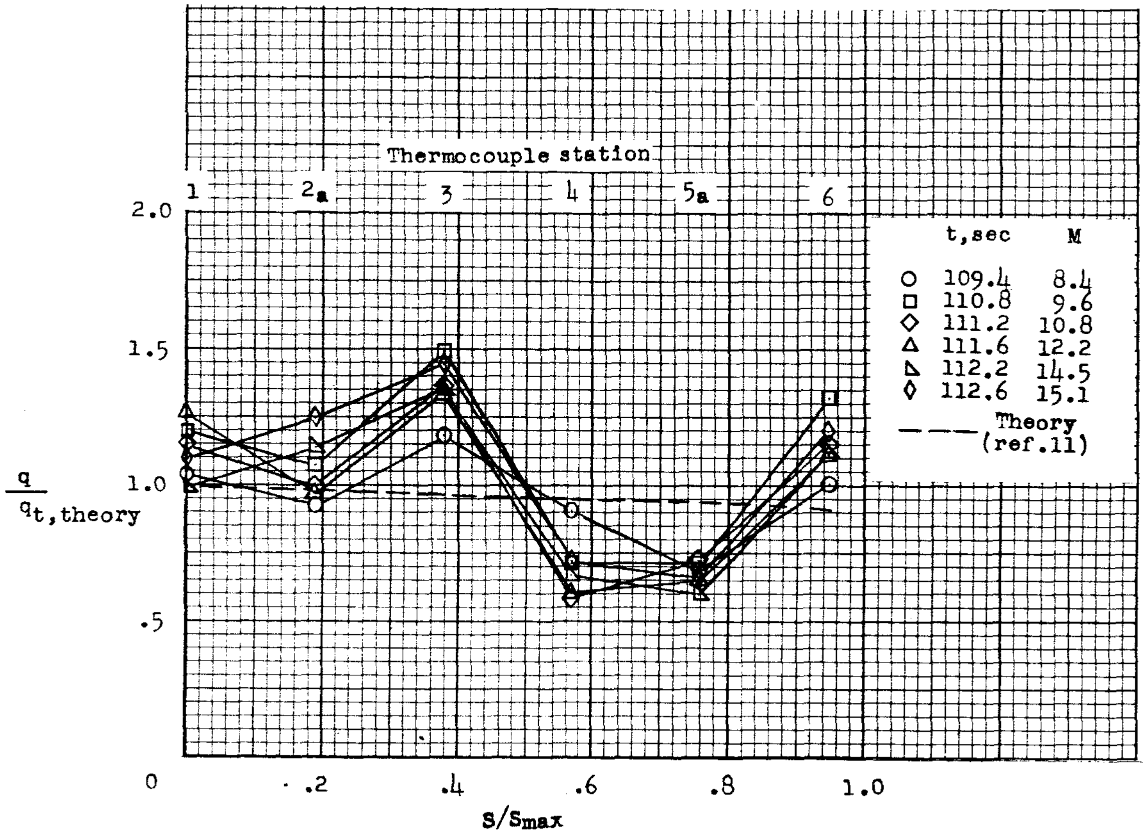

(c) Aerodynamic heating rates as a ratio of theoretical heating rates.

Figure 16.- Concluded.

[redacted]

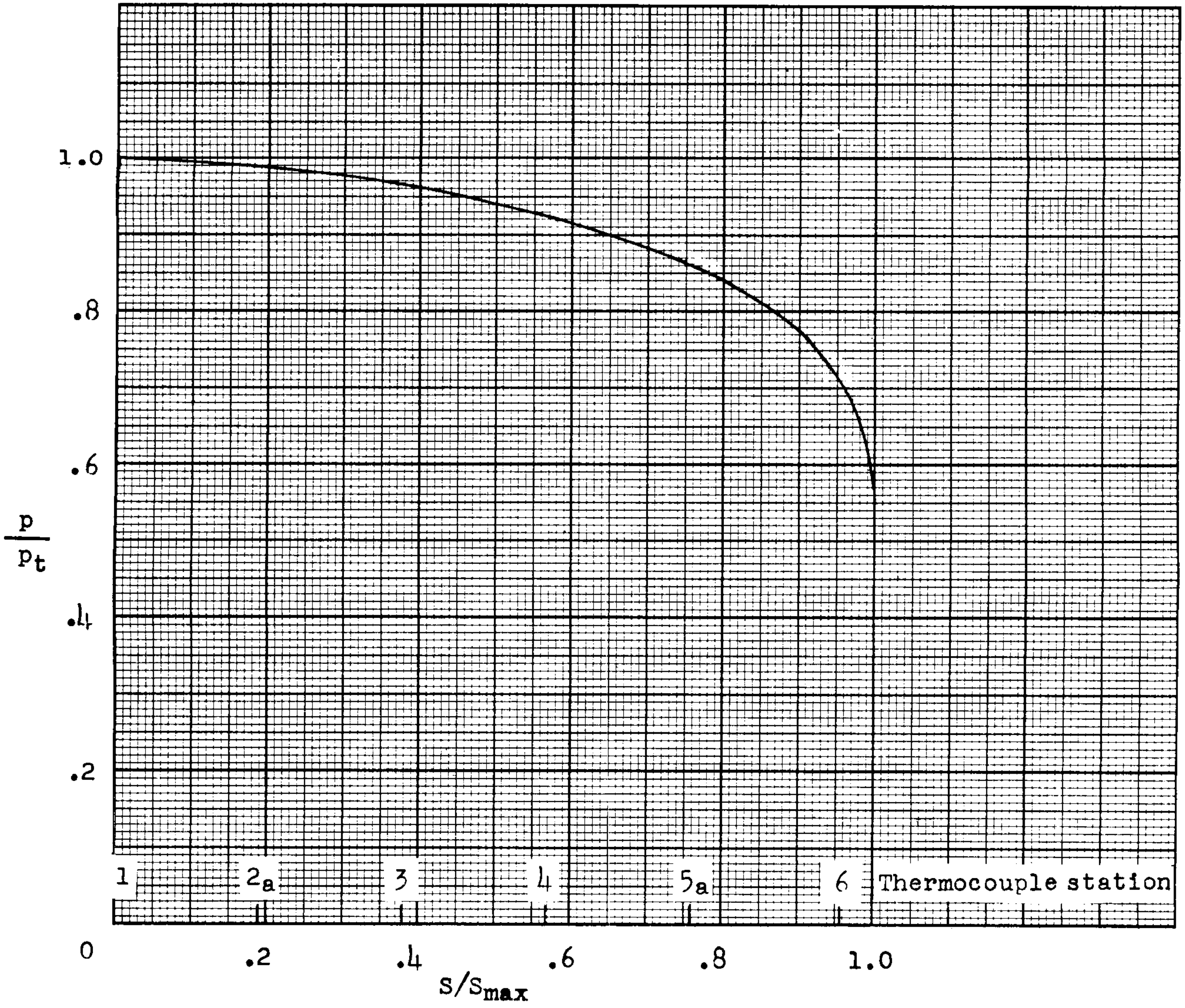

Figure 17.- Pressures from shock tube measurements of reference 12.

[redacted]

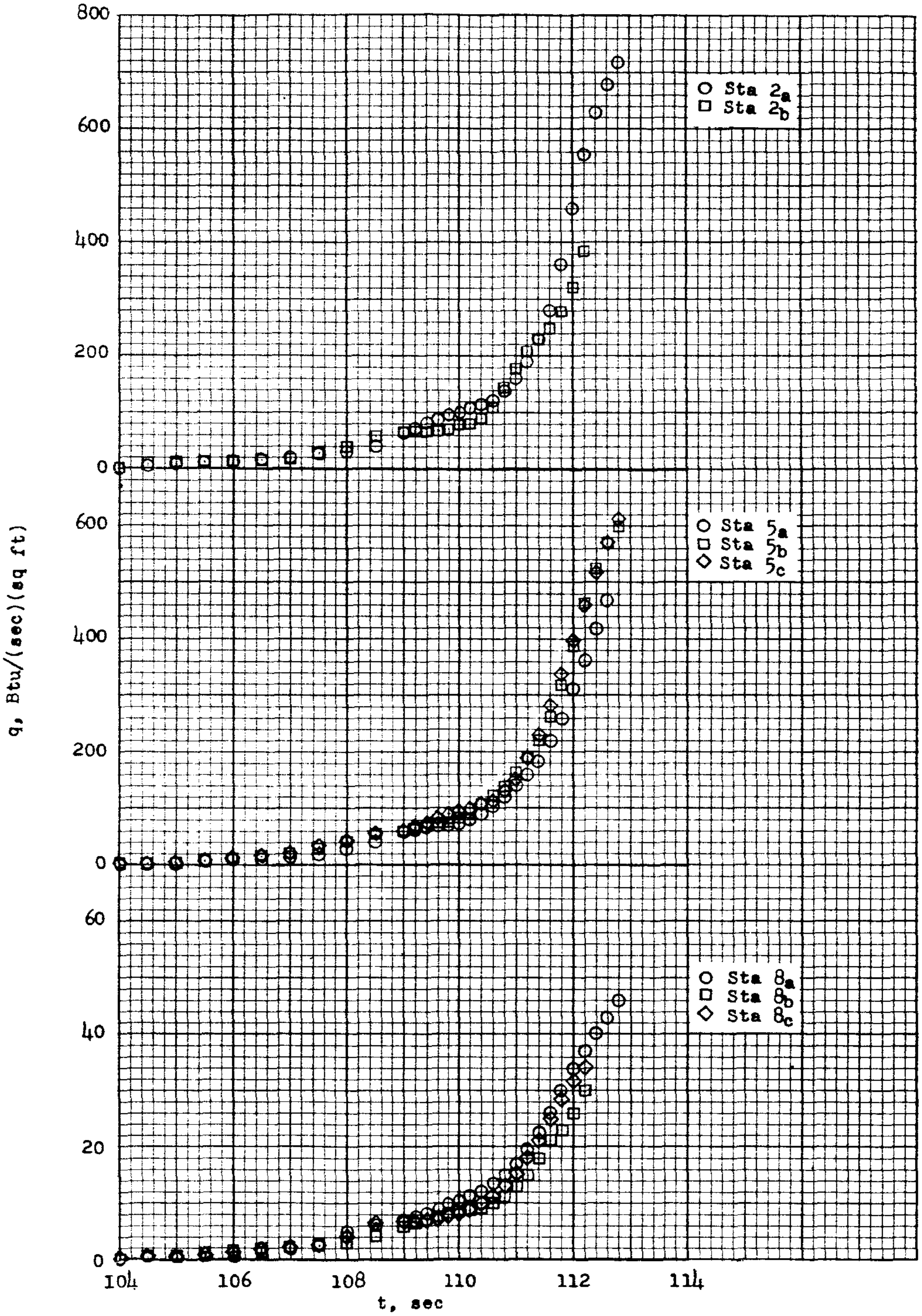

Figure 18.- Comparison of one-dimensional heating rates at axisymmetrical stations.

[redacted]